

Measuring the Geometry and Topology of Large Scale Structure using SURFGEN: Methodology and Preliminary Results

Jatush V.Sheth^{1,4}, Varun Sahni^{1,5}, Sergei F.Shandarin^{2,6} and B.S.Sathyaprakash^{3,7}

¹ *Inter University Centre for Astronomy & Astrophysics, Pune, India*

² *Department of Physics and Astronomy, University of Kansas, KS 66045, USA*

³ *Department of Physics and Astronomy, University of Cardiff, Cardiff, UK*

⁴ *jvs@iucaa.ernet.in*

⁵ *varun@iucaa.ernet.in*

⁶ *sergei@ukans.edu, sergei@ku.edu*

⁷ *B.Sathyaprakash@astro.cf.ac.uk*

22 October 2018

ABSTRACT

Observations of the universe reveal that matter within it clusters on a variety of scales. On scales between 10 - 100 Mpc, the universe is spanned by a percolating network of superclusters interspersed with large and almost empty regions – voids. This paper, the first in a series, presents a new ansatz which can successfully be used to determine the morphological properties of the supercluster-void network. The ansatz is based on a surface modelling scheme (SURFGEN), developed explicitly for the purpose, which generates a triangulated surface from a discrete data set representing (say) the distribution of galaxies in real (or redshift) space. The triangulated surface describes, at progressively lower density thresholds, clusters of galaxies, superclusters of galaxies and voids. Four *Minkowski functionals* (MFs) – surface area, volume, extrinsic curvature and genus – describe the geometry and topology of the supercluster-void network. On a discretised and closed triangulated surface the MFs are determined using SURFGEN. Ratio's of the Minkowski functionals provide us with an excellent diagnostic of three dimensional shapes of clusters, superclusters and voids. Minkowski functionals can be studied at different levels of the density contrast and therefore probe the morphology of large scale structure on a variety of length scales. Our method for determining the Minkowski functionals of a triangulated iso-density surface is tested against both simply and multiply connected eikonal surfaces such as triaxial ellipsoids and tori. The performance of our code is thereby evaluated using density distributions which are pancake-like, filamentary, ribbon-like and spherical. Remarkably, the first three Minkowski functionals are computed to *better than 1%* accuracy while the fourth (genus) is known exactly. SURFGEN also gives very accurate results when applied to Gaussian random fields. We apply SURFGEN to study morphology in three cosmological models, Λ CDM, τ CDM and SCDM, at the present epoch. Geometrical properties of the supercluster-void network are found to be sensitive to the underlying cosmological parameter set. For instance, the percolating supercluster in Λ CDM turns out to be more filamentary but topologically simpler than superclusters in τ CDM and SCDM. It occupies just 0.6% of the total simulation-box volume yet contains about 4% of the total mass. Our results indicate that the surface modelling scheme to calculate Minkowski functionals is accurate and robust and can successfully be used to quantify the topology and morphology of the supercluster-void network in the universe.

Key words: cosmology: theory—structure formation—morphology—superclusters—voids—cosmic web

1 INTRODUCTION

The existence of the supercluster-void network is one of the most intriguing observational features of our universe. Redshift surveys of galaxies confirm that on very large scales the bulk of matter in the universe is concentrated in clusters and superclusters of galaxies which are separated by large almost empty regions, appropriately called voids. At moderate density thresholds $\delta \sim 1$, the supercluster network percolates even though it occupies a tiny fraction of the total volume, and so has a small filling fraction.

The morphology of the supercluster-void network is quite complex and has inspired evocative descriptions such as being ‘honey-comb-like’, ‘bubble-like’, ‘a filamentary network’, ‘swiss cheese’, ‘cosmic web’ etc. Indeed the intricate weave of large scale structure is becoming increasingly evident as results from progressively larger galaxy redshift surveys (CfA, IRAS, PSCz, LCRS, 2dFGRS, SDSS) demonstrate. Quantifying the properties of the supercluster-void network is clearly one of the cardinal tasks facing cosmology today. Since the network evolved from an almost featureless Gaussian random field (as suggested by observations of the cosmic microwave background) it is important to understand how such a rich and complex cosmic tapestry – characterized by prominent non-Gaussian features (clusters, superclusters, voids) – could have arisen from small and statistically random initial conditions. Furthermore, since the network is highly evolved it is unlikely that its principle features can be described within a strictly perturbative framework which breaks down when $\delta \gtrsim 1$. It is therefore both interesting and revealing that approximations which successfully describe non-linear dynamics (such as the Zeldovich approximation and the Adhesion model) generically predict the formation of filaments and pancakes, which interweave and percolate to form the large scale structure of the universe (Shandarin & Zeldovich 1989; Gurbatov, Saichev & Shandarin 1985, 1989). Furthermore, this interweaving network of filaments, sheets and voids – predicted both by the Zeldovich approximation and the adhesion model – is readily seen in N-body simulations of gravitational clustering for a wide variety of initial power spectra (Klypin & Shandarin 1993; Sathyaprakash, Sahni & Shandarin 1996). It therefore appears that a filamentary distribution of large scale structure is an almost generic outcome of pressureless (dark) matter clustering from Gaussian initial conditions. (A theoretical model for understanding the morphology of large scale structure can be found in the “cosmic web” hypothesis of Bond, Kofman & Pogosyan (1996). Insightful overviews of the statistical and dynamical techniques used in studies of large scale structure can be found in: Sahni & Coles (1995); Martinez & Saar (2001); van de Weygaert (2002).)

A number of statistical measures have been advanced to quantify the pattern made by galaxies as they cluster in our universe. Prominent among them are Percolation Analysis (Zeldovich, Einasto & Shandarin 1982; Shandarin & Zeldovich 1983), Counts in Cells (Janes & Demarque 1983; de Lapparent, Geller & Huchra 1991), Minimal Spanning Trees (Barrow, Sonoda & Bhavsar 1985), the Genus measure (Gott, Melott & Dickinson 1986) etc. (To some extent these methods complement the traditional approach to quantify clustering using the hier-

archy of correlation functions (Peebles 1980), which become cumbersome to evaluate beyond the three point function.) Recently Mecke, Buchert and Wagner (1994) have introduced the Minkowski functionals (hereafter MFs) to cosmology. MFs contain information pertaining to geometry, connectivity (percolation) and topology (genus). In addition, the ratio’s of Minkowski functionals quantify the *morphology* of large scale structure. This has led to the construction of a set of measures called Shapefinders which tell us whether the distribution of matter in superclusters/voids is spherical, planar, filamentary etc. (Sahni, Sathyaprakash & Shandarin 1998; Sathyaprakash, Sahni & Shandarin 1998). (Applications of Shapefinders to galaxy catalogues and N-body simulations has been discussed in Basilakos, Plionis & Rowan-Robinson (2000); Kolokotronis, Basilakos & Plionis (2001). Moment-based studies of morphology predating the Shapefinders can be found in Babul & Starkman (1992); Luo & Vishniac (1995).) Thus between them, the four Minkowski functionals contain valuable information regarding both the geometrical as well as topological distribution of matter in the universe. Since Minkowski functionals are additive in nature one can glean information regarding both individual objects (galaxies, clusters, voids) as well as describe the supercluster-void network in its totality.

There have been three major attempts made to study the morphology of the LSS using MFs; these efforts differ in their approach of evaluating the MFs: (1) Firstly, Boolean grain models study the MFs of surfaces which result due to intersecting spheres decorating the input point-set (Mecke, Buchert & Wagner 1994). (2) Secondly, Krofton’s formulae make it possible to calculate MFs on a density field defined on a grid (Schmalzing & Buchert 1997). In this case the MFs are calculated by using the information of the number of cells in 1D (vertices), 2D (faces) and 3D (cuboids). (3) Finally, an alternative, resolution-dependent approach consists in employing the Koenderink invariants (Schmalzing & Buchert 1997, Schmalzing et al. 1999).

This paper introduces a radically new and powerful approach for computing the Minkowski functionals. This approach consists of constructing iso-density surfaces using an elaborate surface modelling scheme defined in terms of excursion sets of a density field. These surfaces are triangulated and the MFs are evaluated for the resulting closed polyhedral surface. A similar algorithm has been used in studies of two-dimensional CMB maps (Novikov, Feldman & Shandarin 1999; Shandarin et al. 2002). However, developing a three-dimensional algorithm requires a new component that builds a surface of approximately constant (to linear order) density. It has been implemented and reported in this paper.

The MFs so constructed are tested against known results for simply connected surfaces (triaxial ellipsoids) as well as multiply connected surfaces (triaxial tori). In all cases we find that our ansatz for determining MFs on polyhedra gives results which are *in excellent agreement* with exact continuum values for these quantities. We have further tested the performance of SURFGEN against Gaussian random fields for which the analytic prediction for MFs is available and find that our calculations reproduce the analytic results to a remarkable precision. This gives us confidence that our ansatz is well suited for application to large N-body

simulations and three-dimensional galaxy redshift surveys. Encouraged by the success on these preliminary tests, we apply our method to simulations of three cosmological models due to the Virgo consortium.

The rest of this paper is arranged as follows: In Section 2, we provide a brief overview of Minkowski functionals and present an algorithm which computes MFs for a triangulated polyhedral surface. In Section 3, we describe the SURFGEN algorithm which triangulates a general class of surfaces including iso-density surfaces describing superclusters or voids. In Section 4 we test our method against standard eikonal surfaces – spheres, ellipsoids, tori – and demonstrate the accuracy of our algorithm. Special boundary conditions are needed to reproduce the analytic expressions for MFs of a Gaussian random field. The related discussion along with the results for Gaussian random fields is presented at the end of the paper in an appendix. Section 5 is devoted to a detailed morphological study of cosmological N-body simulations. The models investigated are Λ CDM, τ CDM and SCDM at the present cosmological epoch. Our conclusions are presented in Section 6 which also discusses possible further applications of SURFGEN and the MFs.

2 MINKOWSKI FUNCTIONALS AND TRIANGULATED SURFACES

The large scale structure of the universe can be studied on various scales by considering the geometry and topology of excursion sets of the density contrast $\delta(\mathbf{x})$ defined as $\mathcal{E}_{TH}^+ = \{\mathbf{x} | \delta(\mathbf{x}) \geq \delta_{TH}\}$, for overdense regions (clusters, superclusters) and $\mathcal{E}_{TH}^- = \{\mathbf{x} | \delta(\mathbf{x}) \leq \delta_{TH}\}$, for underdense regions (voids). By specifying a given density threshold one effectively defines an iso-density surface over which the Minkowski functionals should be evaluated. Depending upon whether the surface encloses overdense region of the space or underdense region, the surface refers to a cluster/supercluster or a void. Note that the term ‘cluster’ is used for any region in the excursion set ($\delta > \delta_{TH}$) which in general is different from the astronomical definition. The terminology reflects the cluster analysis jargon. The following four Minkowski functionals describe the morphological properties of an iso-density surface in three dimensions¹

- [1] *Area* S of the surface,
- [2] *Volume* V enclosed by the surface,
- [3] *Integrated mean curvature* C of the surface (or integrated extrinsic curvature),

$$C = \frac{1}{2} \oint \left(\frac{1}{R_1} + \frac{1}{R_2} \right) dS, \quad (1)$$

where R_1 and R_2 are the principal radii of curvature at a given point on the surface.

- [4] *Integrated intrinsic (or Gaussian) curvature* χ of the surface – also called the *Euler characteristic*

¹ There are $(n + 1)$ Minkowski functionals in n dimensions each defined for an $(n - 1)$ dimensional hypersurface. Two dimensional MFs have been used to analyze the LCRS slices by Bharadwaj et al. (2000) and the anisotropy of the cosmic microwave background by Schmalzing & Gorski (1998) and by Novikov, Feldman & Shandarin (1999).

$$\chi = \frac{1}{2\pi} \oint \left(\frac{1}{R_1 R_2} \right) dS. \quad (2)$$

A related measure of topology is the genus $G = 1 - \chi/2$.² Multiply connected surfaces have $G > 0$ while $G = 0$ for a simply connected surface such as a sphere. (The topological properties of all orientable surfaces are equivalent to those of a sphere with one or more ‘handles’. Thus a torus is homeomorphic to a sphere with one handle, while a pretzel is homeomorphic to a sphere with two handles etc.) While the genus provides information about the connectivity of a surface, the remaining three MFs are sensitive to local surface deformations and hence characterize the geometry and shape of large scale structure at varying thresholds of the density (Sahni, Sathyaprakash & Shandarin 1998).

In nature one seldom comes across surfaces that are perfectly smooth and differentiable. As a result expressions [1] - [4] which make perfect sense for manifolds \mathcal{C}^n , $n \geq 2$ are woefully inadequate when it comes to determining the Minkowski functionals for real data sets which are grainy and quite often sparse. Below we describe how one can determine the Minkowski functionals (and derived quantities) for surfaces derived from real data by interpolation. The interpolation scheme which describes iso-density contours as triangulated surfaces will be presented in detail in the next Section.

We construct a polyhedral surface using an assembly of triangles in which every triangle shares its sides with each of its three neighboring triangles.

- The area of such a triangulated surface is

$$S = \sum_{i=1}^{N_T} S_i, \quad (3)$$

where S_i is the area of the i -th triangle and N_T is the total number of triangles which compose a given surface.

- The volume enclosed by this polyhedral surface is the summed contribution from N_T tetrahedra

$$V = \sum_{i=1}^{N_T} V_i, \quad (4)$$

$$V_i = \frac{1}{3} S_i (n_j \bar{P}^j)_i.$$

Here V_i is the volume of an individual tetrahedron whose base is a triangle on the surface. $(n_j \bar{P}^j)$ is the scalar product between the outward pointing normal \hat{n} to this triangle and the mean position vector of the three triangle vertices, for which the j^{th} component is given by

$$\bar{\mathbf{P}}^j = \frac{1}{3} (P_1^j + P_2^j + P_3^j). \quad (5)$$

The subscript i in (4) refers to the i -th tetrahedron, while the vectors P_1, P_2, P_3 in (5) define the location of each of three triangle vertices defining the base of the tetrahedron relative to an (arbitrarily chosen) origin (Fig. 1). The vertices are ordered anticlockwise. This ensures that the contribution to the volume from tetrahedra whose base triangles

² Genus measures the number of handles in excess of the number of isolated underdense regions (voids) that the surface of a cluster exhibits.

lie on *opposite sides* of the origin add, while the volumes of tetrahedra with base triangles lying on the *same side* of the origin subtract out. Thus for both possibilities we get the correct value for the enclosed volume (Fig. 1).

• The *extrinsic curvature of a triangulated surface is localized in the triangle edges*. As a result the integrated mean curvature C is determined by the formula

$$C = \frac{1}{2} \sum_{i,j} \ell_{ij} \cdot \phi_{ij} \cdot \epsilon, \quad (6)$$

where ℓ_{ij} is the edge common to adjacent triangles i and j and ϕ_{ij} is the angle between the normals to these triangles \hat{n}_i & \hat{n}_j .

$$\cos \phi_{ij} = \hat{n}_i \cdot \hat{n}_j. \quad (7)$$

The summation in (6) is carried out over all pairs of adjacent triangles. It should be noted that for a completely general surface, the extrinsic curvature can be positive at some (convex) points and negative at some other (concave) points on the surface. To accommodate this fact one associates a number $\epsilon = \pm 1$ with every triangle edge in (6). $\epsilon = 1$ if the normals on adjacent triangles diverge away from the surface, indicating a locally convex surface, while $\epsilon = -1$ if the normals converge towards each other outside the surface, which is indicative of a concave surface. In the former case the centre of curvature of the surface lies within the surface-body whereas in the latter case the centre of curvature lies outside of the surface-body (Fig. 2).

• The genus of a triangulated closed polyhedral surface is given by the convenient expression

$$G = 1 - \frac{\chi}{2}, \quad \chi = N_T - N_E + N_V, \quad (8)$$

where χ is the Euler characteristic of the triangulated surface. N_T, N_E, N_V are, respectively, the total number of triangles, triangle-edges, and triangle-vertices defining the surface.

• As demonstrated in Sahni, Sathyaprakash & Shandarin (1998); Sathyaprakash, Sahni & Shandarin (1998) ratio's of Minkowski functionals called ‘‘Shapefinders’’ provide us with an excellent measure of morphology. Therefore, in addition to determining MFs we shall also determine the Shapefinders, T (Thickness), B (Breadth) and L (Length) which are defined as follows:

$$T = \frac{3V}{S}, \quad B = \frac{S}{C}, \quad L = \frac{C}{4\pi(G+1)}, \quad (9)$$

where $G = 0$ for simply connected surfaces and $G > 0$ for multiply connected regions. The three Shapefinders (describing an object) have dimensions of length and provide us with an estimate of the ‘extension’ of the object along each of the three spatial directions: T is the shortest and thus describes the characteristic thickness of the object, L is the longest and thus characterizes the length of the object; B is intermediate and can be associated with the breadth of the object. This simple interpretation obviously is relevant only for fairly simple shapes. For example, a triaxial ellipsoid has the values of T , B and L closely related to the lengths of the three principal axes: shortest, intermediate and the longest respectively. It is worth stressing that L defined by eq. (9) quantifies the characteristic length between

holes which should be taken into account when interpreting the results (e.g. Table 3 below).

• An excellent indicator of ‘shape’ is provided by the dimensionless Shapefinder statistic

$$P = \frac{B-T}{B+T}, \quad F = \frac{L-B}{L+B}, \quad (10)$$

where P and F are measures of Planarity and Filamentarity respectively ($P, F \leq 1$). A sphere has $P = F = 0$, an ideal filament has $P = 0, F = 1$ while $P = 1, F = 0$ for an ideal pancake. Other interesting shapes include ‘ribbons’ for which $P \sim F \sim 1$. When combined with the genus measure, the triplet $\{P, F, G\}$ provides an example of *shape-space* which incorporates information about topology as well as morphology of superclusters and voids.³

Having presented an ansatz to calculate MFs and Shapefinders on a triangulated surface, we now discuss the *surface generating* algorithm (SURFGEN) which creates triangulated surfaces corresponding to iso-density contours evaluated at any desired threshold of the density field.

3 SURFACE GENERATING ALGORITHM (SURFGEN)

SURFGEN is a versatile and powerful prescription which allows us to generate and study surfaces whose physical origin can be quite varied and different. Intensity surfaces (isophotes), isotherms and iso-density surfaces constructed from 3D data provide examples of two dimensional surfaces which can be generated and studied using SURFGEN and the Minkowski functionals discussed in the previous section⁴. The present paper is the first of a series in which SURFGEN and MFs will be used in conjunction to make a detailed morphological study of the supercluster-void network in the universe. SURFGEN will be applied to a density field $\rho(\mathbf{r})$ defined on a rectangular cubic lattice.

The SURFGEN algorithm is constructed as follows:

(i) A point particle distribution (from N-body simulations, galaxy catalogues) is used to reconstruct the density field on the vertices of a cubic lattice via a cloud-in-cell (CIC) approach. The lattice itself consists of a large number of closely packed elementary cubes. Any given cube is characterized by the value of the density at its eight vertices.

(ii) An appropriate density threshold ρ_{TH} is chosen and lattice points at this threshold are found using linear interpolation. The lattice-cells which involve such interpolated points along their sides are marked for triangulation which is to be done in the next step.

(iii) SURFGEN determines a closed polyhedral surface at the threshold ρ_{TH} by *triangulating elementary cubes* while

³ Non-geometrical shape-statistics based on mass moments etc. can give misleading results when applied to large scale structure, as demonstrated in Sathyaprakash, Sahni & Shandarin (1998).

⁴ SURFGEN is a modified and extended version of the Marching Cubes Algorithm (MCA) which is used in the field of medical imaging to render high resolution images of internal organs by processing the output generated by X-ray tomography (Lorenson & Cline 1987).

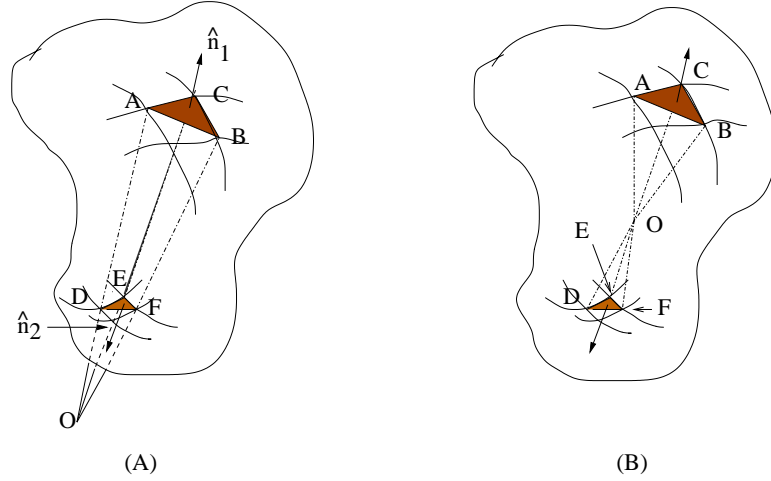


Figure 1. Volume enclosed by the surface is estimated by *vectorially* summing over the volumes of individual tetrahedra; each having its base at one of the triangles composing the surface; and its apex at an arbitrarily chosen point which we call the origin. Note that the origin can lie both within as well as outside the surface. The left panel shows how SURFGEN estimates the volume when the origin lies *outside* the surface. In this case, the contribution (to the enclosed volume) from triangles falling in the same solid angle carries opposite sign for tetrahedra OABC and OFED. Clearly the volume of OFED must be subtracted from the volume OABC in order to give the true volume enclosed by the surface. Anticlockwise orientation of the vertices used in determining the normals of the base triangles helps us bring this about. The right panel shows the second possibility for which the two triangles ACB and DEF form tetrahedra whose fourth (common) vertex lies *within* the surface. In this case, the contributions from ODEF and OACB add to give the total volume.

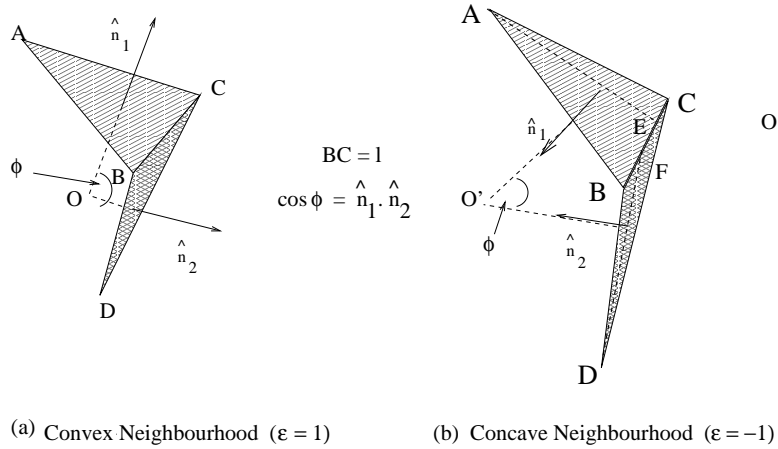


Figure 2. Illustrated here is the algorithm to compute the local contribution to the Integrated Mean Curvature: (a) $\triangle ABC$ and $\triangle CBD$ are two triangles sharing a side BC of length ℓ . The normals \hat{n}_1 and \hat{n}_2 to the two triangles lie in the planes orthogonal to BC . Their projection in the plane of the paper diverges from a point O *inside* the surface. Thus the triangles correspond to a convex neighborhood and $\epsilon = 1$ in Eq.(6). The angle between the two triangles is denoted as ϕ . (b) Shown here are a similar pair of triangles, but with inverted sense of the normals, so that the sense of the surface is opposite to that shown in (a). We note that in the present case, the two normals converge *outside* the surface, so that their projections in the plane of the paper would meet at O' , which lies outside the surface. Thus this represents a concave neighborhood, for which $\epsilon = -1$ in Eq.(6). The angle ϕ represents the internal angle between \hat{n}_1 and \hat{n}_2 .

simultaneously moving across the lattice. Triangulated elementary cubes are then put together to make up the full two-dimensional triangulated surface.

The process of triangulation is based on the following observation.

For any arbitrary threshold of the density, all elementary cubes of the density field fall into one of the following three classes:

- (i) those which have all eight vertices below the density threshold (*underdense cubes* – Fig. 3–I),
- (ii) those which have all eight vertices above the density threshold (*overdense cubes* – Fig. 3–II),
- (iii) cubes having both overdense and underdense vertices (*surface cubes* – Fig. 3–III).

When modelling clusters and superclusters overdense cubes will be *enclosed* by our surface while underdense cubes will be excluded by it. (For voids the situation will be reversed.) Contour surfaces at a prespecified density thresh-

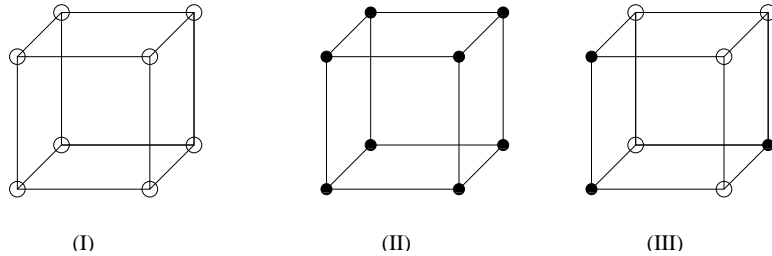


Figure 3. Given a density field defined on a lattice, the elementary lattice-cubes fall into one of the above three classes: (1) The cubes which are completely underdense, (2) the cubes which are completely overdense and finally (3) such cubes which have a few vertices overdense and the remaining vertices underdense. Cubes referring to the 3rd category are triangulated to model the surfaces.

old will *lie entirely within surface cubes*. Thus the properties of *surface cubes* are vitally important for this surface-reconstruction exercise.

We now describe how SURFGEN constructs a surface at the desired threshold ρ_{TH} by triangulating *surface cubes*. We work under the assumption that the underlying density field $\rho(\mathbf{r})$ is continuous, so that in moving from an overdense site to an underdense site (along a cube edge) we invariably encounter a point at which $\rho = \rho_{TH}$. SURFGEN classifies a given lattice-cube in terms of the number of points (on the edges) where $\rho = \rho_{TH}$. The precise location of these points (found by interpolation) tells us exactly where our iso-density surface will intersect the cube. Since there are eight vertices and each vertex can either be overdense (1) or underdense (0), the number of possible configurations of the cube are $2^8 = 256$. Clearly the triangulation must be invariant upon interchanging 1's with 0's, and this reduces the number of independent configurations to 128. Upon invoking rotational symmetry this number further reduces to only 14. (For instance, although there are eight cubes which have a single overdense vertex, any two members of this family are related via the three dimensional rotation group. Therefore a single scheme of triangulation suffices to describe all members of this group.) These fourteen configurations of triangulated cubes are shown in Fig. 4 (also see Lorenson & Cline (1987)).

The surface intersecting a given *surface cube* forms quite clearly only a portion of the full iso-density surface which we are interested in constructing. By explicitly demanding that the density field be *continuous* across the iso-density surface one joins triangles across the faces of neighboring cubes, thus constructing the full continuous polyhedral surface. This then is the basic prescription which may be used to construct a closed triangulated surface at any desired value of the density threshold. However, a few comments about triangulation are in order: (i) the triangulation of the cubes having four contrasting vertices is *not unique*. To illustrate this let us consider Fig. 5 where the last cube belonging to the middle row of Fig. 4 is reproduced in the left panel. We note that this cube is symmetric with respect to an interchange of underdense sites with overdense sites. As a result, we could just as well triangulate it according to the prescription shown in the right panel of Fig. 5. This degeneracy in the way a given cube can be triangulated is inherent also in the last two cubes of the last row of Fig. 4. Noticeably, at all such places where we encounter one of these cubes, one scheme of triangulation has to be preferred over the other, otherwise the surface could become discontinuous. Thus to

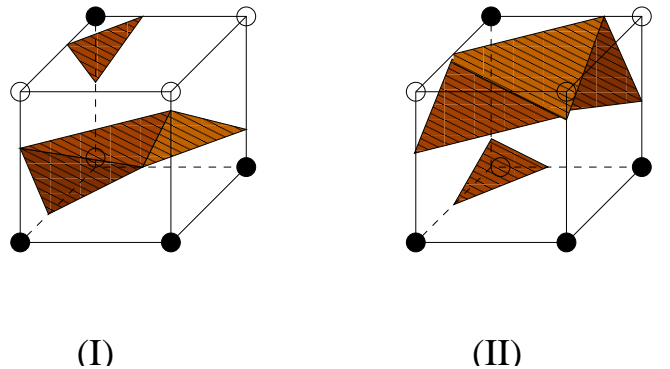


Figure 5. The cube shown here is the last in the middle row of Fig. 4. It has four overdense and underdense vertices and, as shown above, it can be triangulated in two distinct ways. Two other cubes (not shown) also allow for this possibility (of being triangulated in two distinct ways). These are the last two cubes belonging to the last row of Fig. 4. The original MCA algorithm does not mention this degeneracy. However, it can be shown that this degeneracy can be broken if we include information about neighboring cubes. Requiring that the density field be continuous across the neighboring cubes breaks an occasional degeneracy which may arise, and allows one to triangulate surfaces unambiguously.

create a unique triangulated surface one must triangulate such cubes *in tandem* with their neighbors, ensuring that the continuity of the surface is maintained. (ii) There are instances when two neighboring cubes have a density configuration which does not lead to the complete closure of the given surface. The resulting surface has a hole (Fig. 6a) which must be filled by constructing two additional triangles which close the surface (Fig. 6b). The probability of hole formation is finite every time the common face shared by two cubes shows two vertices of type 1 along one diagonal and of type 0 along the other diagonal.

Thus, in order to generate a closed polyhedral surface at a given value of the density threshold $\rho = \rho_{TH}$ SURFGEN uses the 14 independent triangulations of an elementary lattice cube in conjunction with an algorithm which ensures that the surface is continuous. We should emphasize that surfaces generated in this manner *need not be simply connected* (see Fig. 7). Indeed iso-density surfaces constructed at moderate density thresholds in N-body simulations as well as 3D galaxy surveys tend to show a large positive value for the genus (Eq. 8). This issue will be discussed in detail in forthcoming paper(s). To enable an online calculation of

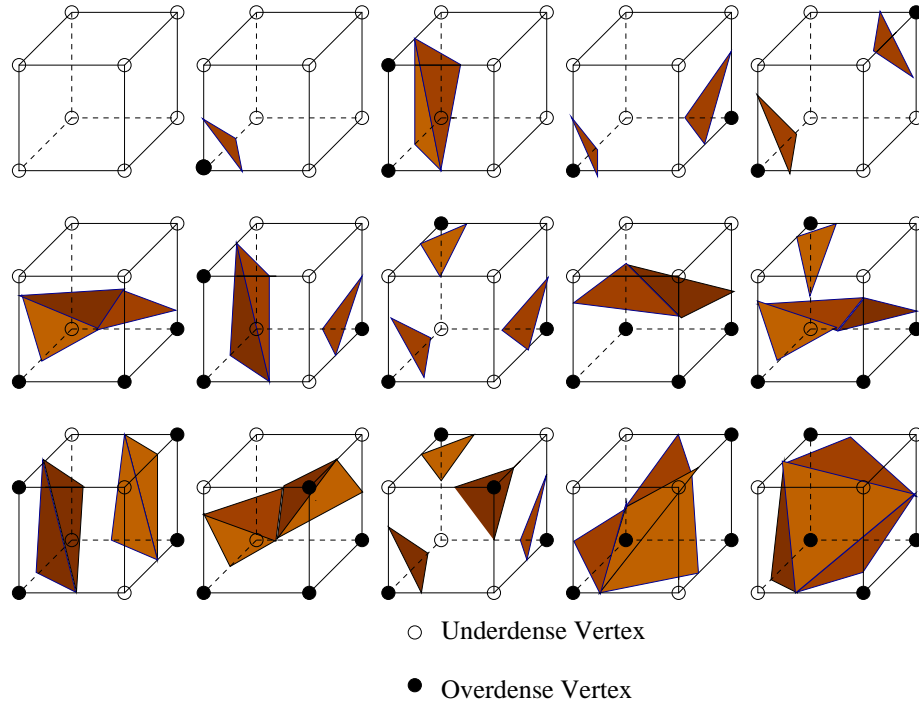


Figure 4. Depending upon the value of density (or temperature, if isotherms are being constructed and photon counts, if isophotes are being modelled) at its vertices, a surface cube can be triangulated according to one of the fourteen independent configurations shown above. The black dots represent overdense vertices whereas underdense vertices are represented by open circles.

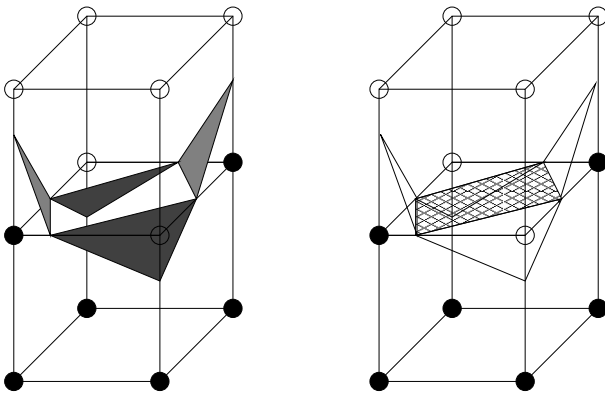


Figure 6. Formation of a ‘hole’ is illustrated. We ‘fill’ this hole by a pair of triangles as shown in the right panel of the figure. Since the original MCA algorithm was meant strictly for visualization purposes, this problem appears to have been overlooked in Lorenson and Cline (1987). We correct for this in our triangulation scheme by filling holes whenever they occur since its of prime importance to work with closed polyhedral surfaces when constructing MFs.

the MFs, our surface modelling scheme also adheres to the following requirements:

- The vertices of all the triangles are stored in an anticlockwise order. This enforces a uniform prescription on normals which always point outward from the surface being modelled. Information regarding the directionality of normals is of great importance since it is used both for calculating the volume as well as the mean curvature.
- For online calculation of the mean curvature, informa-

tion concerning a given triangle must be supplemented with information concerning the triplet of triangles which are its neighbors. This allows us to unambiguously determine the contribution to the mean curvature from a local neighborhood.

- The total number of triangles, triangle-edges and triangle-vertices of a triangulated surface are counted which enable us to determine its genus when surface construction is complete.

We might add that, although in this paper the density field is reconstructed from N-body particle positions by means of a CIC prescription, this is not a necessary prerequisite for SURFGEN which is versatile enough to be used to triangulate iso-density contours of fields reconstructed using more elaborate techniques such as Delaunay tessellations (Schaap & Weygaert 2000; van de Weygaert 2002), Wiener reconstruction or adaptive smoothing. As it turns out, these schemes tend to maintain the structural complexity in the system without diluting the patterns in an isotropic manner. However, since SURFGEN constructs a triangulated surface by ‘marching across neighboring lattice cubes’ (Lorenson & Cline 1987) the density field must be specified on a cubic lattice for this approach to give meaningful results.⁵

To summarize, our surface modelling code incorporates the triangulation of the entire set of 256 possible configura-

⁵ We should emphasize however that the ansatz developed in section 2 for determining the Minkowski functionals for a triangulated surface can easily be adapted to other triangulation schemes such as those described in O’Rourke (1998); van de Weygaert (2002).

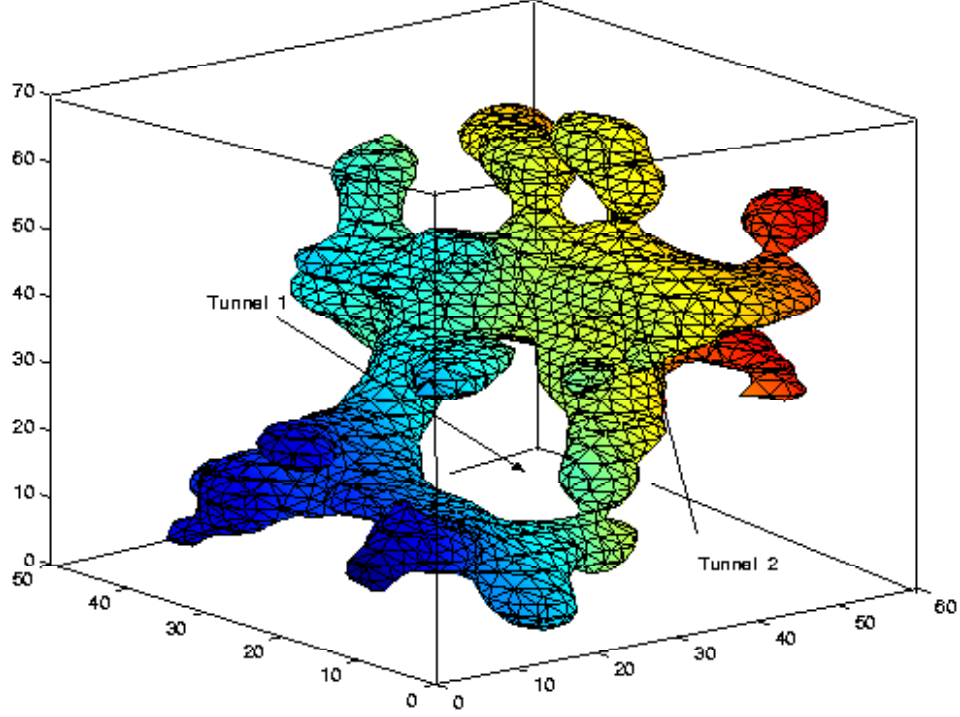


Figure 7. A cluster appearing in the Λ CDM simulation is triangulated using SURFGEN. The cluster is multiply connected with two tunnels and hence is described by a genus value of two.

tions of a cube within a single scheme and makes possible online computation of the area, the volume, the integrated mean curvature and the genus of a triangulated surface. The code has been tested on a variety of standard density distributions and eikonal morphologies as well as on Gaussian random fields. In the next section, we present results based on this analysis.

4 RESULTS FOR STANDARD EIKONAL SURFACES

In order to test the accuracy of our ansatz we generate triangulated surfaces whose counterpart continuum surfaces have known (analytically calculable) Minkowski functionals.

4.1 Spherical structures

In the first exercise, we consider spherically symmetric density distributions and generate surfaces of constant density for a variety of density-thresholds starting from a chosen maximum radius down to grid-size. A convenient density distribution for this exercise is

$$\rho(i, j, k) = \begin{cases} \frac{\rho_0}{R}, & (i, j, k) \neq (i_0, j_0, k_0), \\ \rho_0, & (i, j, k) = (i_0, j_0, k_0), \end{cases} \quad (11)$$

where R is the distance between (i, j, k) and the centre.

$$R = \sqrt{(i - i_0)^2 + (j - j_0)^2 + (k - k_0)^2}. \quad (12)$$

Since the density field falls off as the inverse of the distance from the centre at (i_0, j_0, k_0) , any threshold ρ_{TH} is associated with a sphere of radius $R = \frac{\rho_0}{\rho_{TH}}$. Thus larger

spheres correspond to surfaces of lower constant density in this model. We assume $i_0 = j_0 = k_0 = 15$, for the centre of the sphere in our numerical calculations.

Applying the Shapefinders (9) & (10) to a sphere of radius R one finds the simple result $T = B = L = R$ and $F = P = 0$. Figure 8 compares the area, volume, mean curvature and Shapefinders measured for a triangulated sphere against known analytical values for these quantities. This figure clearly demonstrates that exact values, and values computed using triangulation, match exceedingly well down to the very lowest scale.

We should mention that the Genus evaluated using Eq.8 is identically zero for spheres of all radii and for all possible deformations of an ellipsoid (to be discussed next). This provides an excellent independent endorsement of our methodology by demonstrating that our triangulations of a sphere and ellipsoid indeed result in closed, continuous surfaces.

4.2 Triaxial ellipsoid

A triaxial ellipsoid is an excellent shape with which to test a morphological statistic. This is because, depending upon the relative scales of the three axes, a triaxial ellipsoid can be oblate, prolate or spherical. We saw previously that MFs and Shapefinders give extremely accurate results for spherical surfaces. We now demonstrate that this remains true even for surfaces which are highly planar or filamentary.

The parametric form of an ellipsoid having axes a , b , c and volume $V = \frac{4\pi}{3}abc$ is

$$\mathbf{r} = a(\sin \theta \cos \phi)\hat{x} + b(\sin \theta \sin \phi)\hat{y} + c(\cos \theta)\hat{z} \quad (13)$$

where $0 \leq \phi \leq 2\pi$, $0 \leq \theta \leq \pi$. For the purposes of our study,

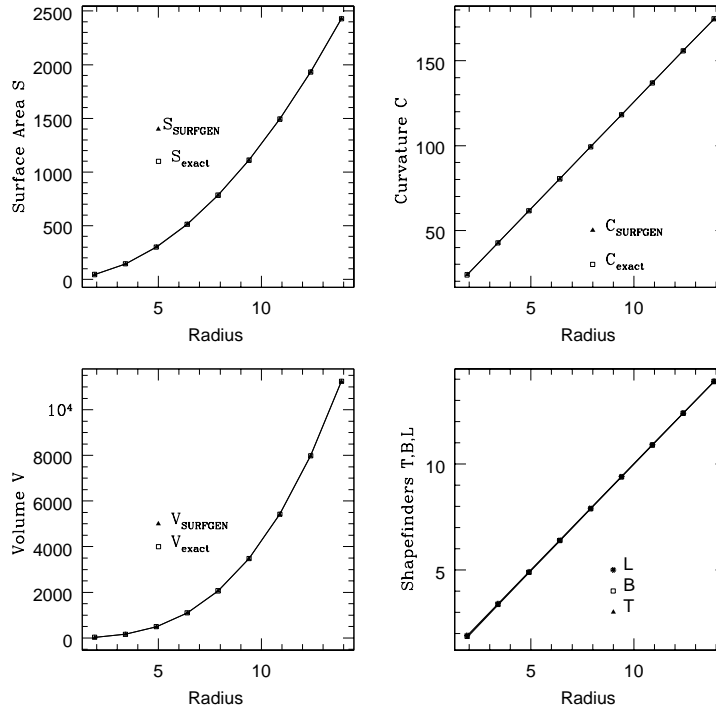


Figure 8. Minkowski Functionals and dimensional Shapefinders for a sphere. Note that the results for the Minkowski Functionals evaluated using our surface modelling scheme (SURFGEN) virtually coincide with the exact values.

we systematically deform a triaxial ellipsoid and study how its shape evolves in the process. When shrunk along a single axis a triaxial ellipsoid becomes planar. Simultaneous shrinking along a second axis makes it cigar-like or filamentary.

4.2.1 Oblate spheroids

We first study the accuracy of our triangulation scheme for planar configurations by considering oblate deformations of an ellipsoid. In this case two axes a and b are held fixed ($a \sim b$), while the third axis c is slowly shrunk leading to an increasingly planar surface. Our results for this case are compiled in two figures. Figure 9 shows MFs as they evolve with the dimensionless variable c/a . (The exact results for the Minkowski functionals which we quote are based on the analytical expressions for MFs given in Sahni, Sathyaprakash & Shandarin (1998), we refer the reader to that paper for more details.) Figure 9 clearly demonstrates that the values of MFs obtained using triangulation match the exact values to a remarkable degree of accuracy. Indeed, for a wide range in c/a the two distinctly different calculational algorithms give virtually indistinguishable results, thereby indicating that the triangulation ansatz is, for all practical purposes, exact!

Figure 10 shows the evolution of all the Shapefinders, i.e., T, B, L, P and F together with the percentage errors in the estimation of dimensional Shapefinders. We find that L is estimated to greatest accuracy with maximum error of $\sim 0.4\%$, while T and B can be determined to an accuracy of $\sim 0.8\%$. We further note (right panels of Figure 10) that

Planarity grows from an initially low value ~ 0.0 to a large final value ~ 0.4 as the ellipsoid becomes increasingly oblate. Filamentarity, on the other hand remains small at ~ 0.09 . Both Filamentarity and Planarity are determined to great accuracy by SURFGEN.

4.2.2 Prolate spheroids

Next we study prolate deformations of our oblate ellipsoid. We start with $b \simeq a, c \ll a$, and shrink the second axis b while keeping a and c fixed, so that finally $c \sim b \ll a$ and our initially oblate ellipsoid becomes prolate. Our results are again summarized in two figures.

Figure 11 reveals very good agreement between measured and true values of MFs, with the former tending to be slightly smaller than the latter.

Turning to the Shapefinders we find that, with the possible exception of extremely prolate figures, the Shapefinders are remarkably well determined. Indeed, even the extremely prolate ellipsoid with axis ratio $b/a < 0.2$ has a largest error in T of only $\sim 1.7\%$ while errors in B and L never exceed $\sim 1\%$ (Fig. 12). This figure also shows the evolution of planarity (P) and filamentarity (F) as our ellipsoid becomes increasingly more prolate. In keeping with our expectation F steadily increases from a small initial value ~ 0.1 to ~ 0.44 . Planarity drops from its large initial value to a small final value $P \sim 0.1$ and is slightly underestimated for $b/a \gtrsim 0.3$. We therefore conclude that both P and F are determined by SURFGEN to a sufficient accuracy for prolate ellipsoidal figures.

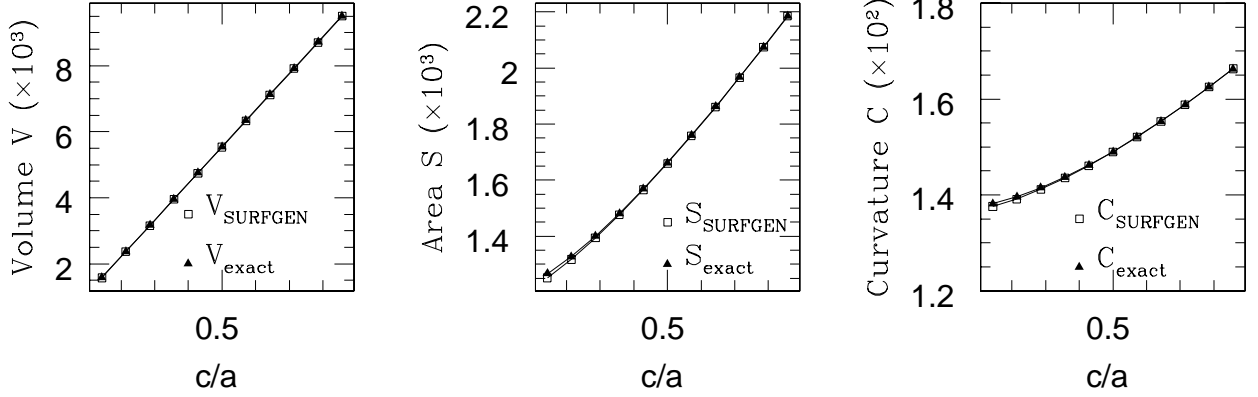


Figure 9. Values of Minkowski functionals determined by the surface modelling scheme SURFGEN are shown along with their exact values for oblate deformations of an ellipsoid. Note that for $c/a > 0.2$, values for Minkowski Functionals evaluated using SURFGEN virtually coincide with the exact results.

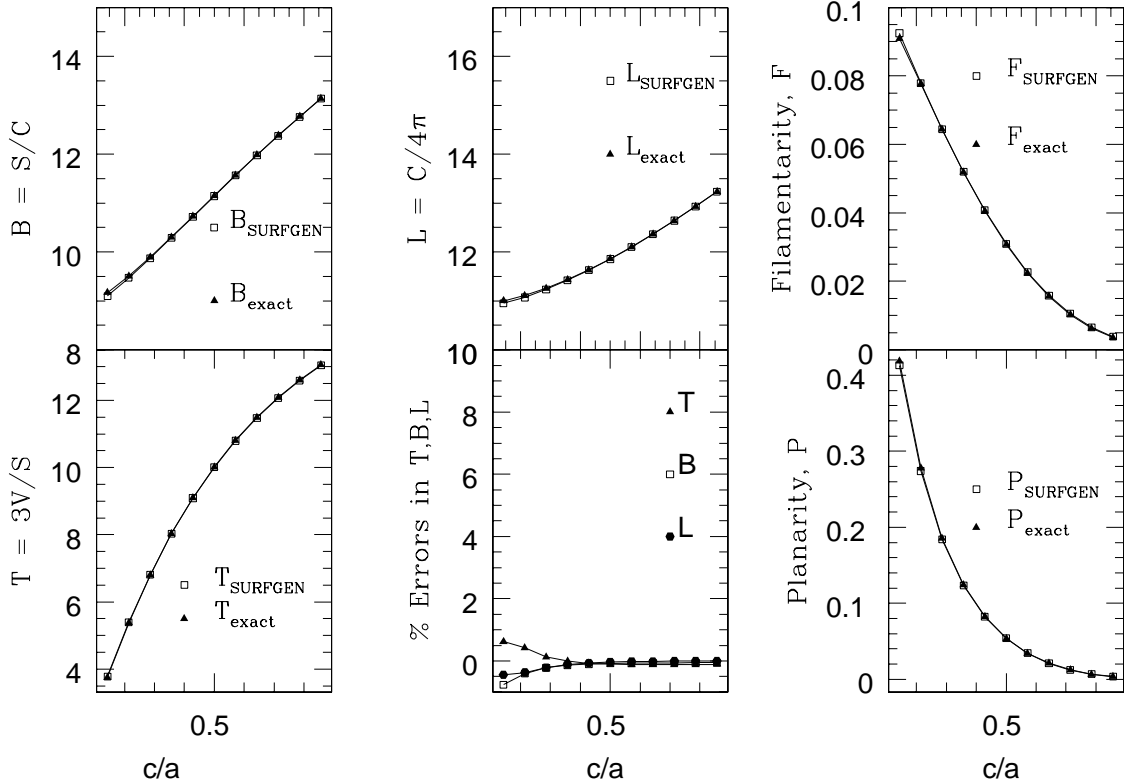


Figure 10. Values of Shapefinders derived using the surface modelling scheme SURFGEN are shown along with their exact values for oblate deformations of an ellipsoid. The lower middle panel shows percentage errors in the estimation of these quantities. We note that the errors are all in the range of $\pm 0.9\%$. The right panels show the evolution of planarity and filamentarity with continuous shrinking of c -axis of the ellipsoid. Note that planarity increases from its low initial value whereas there is only a marginal increase in filamentarity.

4.3 The Torus and its deformations

Next we extend our analysis to manifolds which are multiply connected by considering the deformations of a torus which has an elliptical cross section and which we shall refer to as an elliptical torus. A torus is an important surface on which

to test SURFGEN for two reasons: it is multiply connected and, unlike an ellipsoid, it contains regions which are convex (on its outside) as well as concave (on its inside). The elliptical torus can be described by three parameters a, b, c . In this case the elliptical toroidal tube has diameter $2\pi b$ and a & c are its radii of curvature in two mutually orthogonal

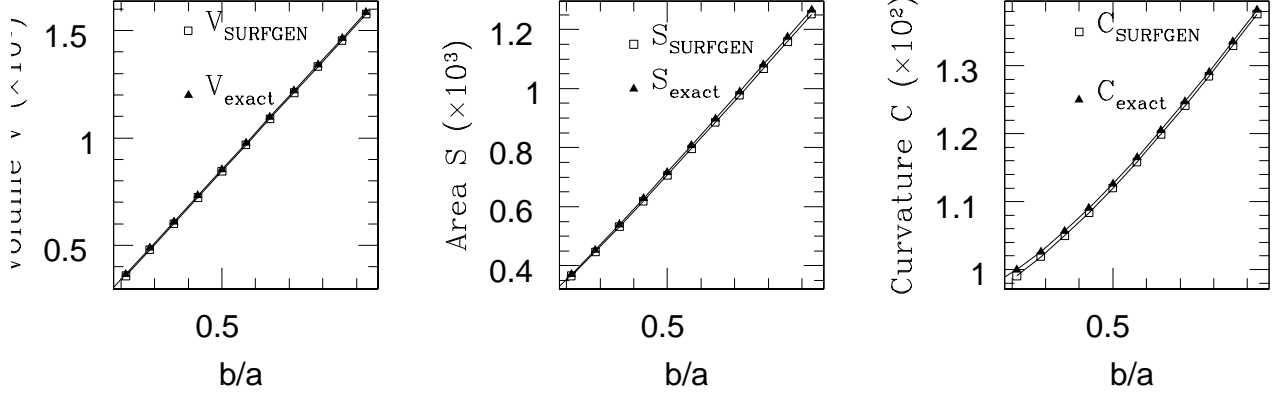


Figure 11. Values of Minkowski functionals determined by the surface modelling scheme SURFGEN are shown along with their exact values for prolate deformations of an ellipsoid. Note that for $b/a \geq 0.3$, the results for the Minkowski Functionals evaluated using SURFGEN virtually coincide with the exact values.

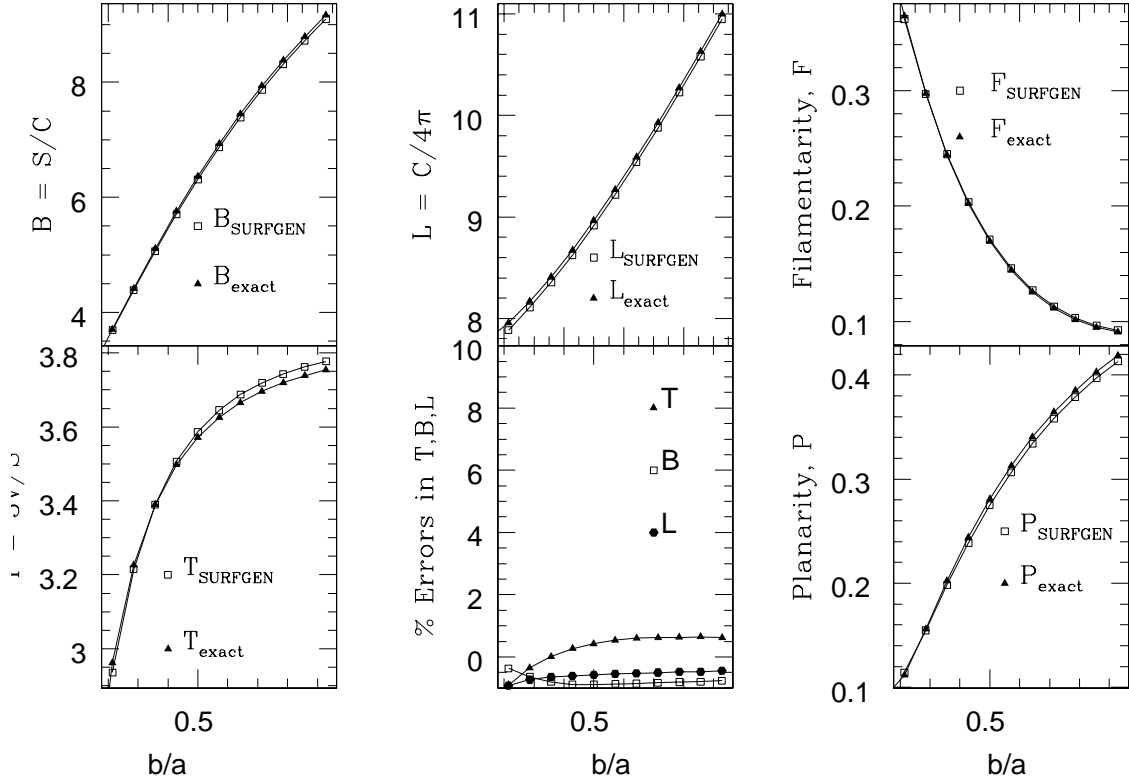


Figure 12. Values of the dimensional Shapefinders derived from the surface modelling scheme SURFGEN are shown along with their exact values for prolate deformations of an ellipsoid. The lower middle panel shows percentage errors in the estimation of these quantities. We note that the error in the estimation of all the quantities lies within +1% to -2%. The right panels show the evolution of planarity and filamentarity with continuous shrinking of the b-axis. Note that the planarity decreases from its high initial value and the filamentarity increases steadily.

directions. The elliptical torus reduces to the more familiar circular torus when $a = c$. We choose to work with the elliptical torus because changing the values of a, b, c can give rise to a large variety of surfaces all of which (by definition) are multiply connected but which have very different shapes.

Thus our surface modelling scheme SURFGEN can be put to a rigorous test. The parametric form for the elliptic torus is

$$\mathbf{r} = (b + c \sin \phi) \cos \theta \hat{x} + (b + c \sin \phi) \sin \theta \hat{y} + a \cos \phi \hat{z}, \quad (14)$$

Table 1. Minkowski Functionals for some extreme deformations of an elliptical torus. $\frac{\Delta C}{C}$, $\frac{\Delta S}{S}$ and $\frac{\Delta V}{V}$ give the percentage error in the determination of the Minkowski functionals (MFs) using SURFGN. An accuracy of better than 1% is achieved for the three MFs: Curvature (C), Surface area (A) and Volume (V), while the genus is determined exactly.

b, a, c	Surface	C	$\frac{\Delta C}{C}\%$	S	$\frac{\Delta S}{S}\%$	V	$\frac{\Delta V}{V}\%$	Genus
(40.0,37.9,37.9)	Sphere-with-hole	7.93×10^2	+0.47	5.98×10^4	-0.01	1.13×10^6	-0.001	1
(140.0,19.9,1.99)	Ribbon	2.8×10^3	+0.03	7.1×10^4	-0.42	1.1×10^5	-0.830	1
(60.0,57.9,3.86)	Pancake	1.2×10^3	+0.40	8.8×10^4	-0.18	2.7×10^5	+0.590	1
(50.02, 3.52, 3.52)	Filament	9.92×10^2	+0.52	6.95×10^3	+0.18	1.21×10^4	-0.580	1

Table 2. SURFGN determined values of the Shapefinders T (Thickness), B (Breadth), L (Length), P (Planarity) and F (Filamentarity) describing extreme deformations of an elliptical torus. Also given alongside are the percentage errors in their estimation.

Surface	T	$\frac{\Delta T}{T}\%$	B	$\frac{\Delta B}{B}\%$	L	$\frac{\Delta L}{L}\%$	P	$\frac{\Delta P}{P}\%$	F	$\frac{\Delta F}{F}\%$	Genus
Sphere-with-hole	56.86	0.02	75.44	-0.48	31.57	0.48	0.140	-1.41	-0.410	0.95	1
Ribbon	4.67	1.08	25.63	-0.47	109.96	0.03	0.692	-0.57	0.622	0.32	1
Pancake	9.09	0.74	74.19	-0.59	47.11	0.41	0.782	-0.26	-0.223	2.19	1
Filament	5.23	-0.95	7.01	-0.43	39.49	0.46	0.145	1.40	0.698	0.28	1

where $a, c < b$, $0 \leq \phi < 2\pi$ and $\theta < 2\pi$. We shall compare results due to SURFGN with the exact analytical results for four kinds of tori - a nearly spheroidal torus, a ribbon, a pancake, and a filament. Tables 1 and 2 refer to these four surfaces; relevant figures can be found in Sahni, Sathyaprakash & Shandarin (1998). Table 1 shows the estimated values of the Minkowski Functionals and the percentage error in their estimation. Table 2 shows all the Shapefinders for these surfaces⁶. This table also shows the percentage errors in the estimation of the Shapefinders.

We should emphasize that the genus estimated by SURFGN for all these deformations has the correct value of unity. This gives an important independent check on the self-consistency of the triangulation scheme since, the absence of even a single triangle out of several thousand, would create an artificial ‘hole’ in our surface and give the wrong value for the genus – a situation that has *never* occurred for any of the several dozen deformations of either the ellipsoid or the torus.

Our results clearly demonstrate that the surface modelling scheme SURFGN provides values for the Minkowski functionals which are in excellent agreement with exact analytical formulae. We have further tested SURFGN against a set of Gaussian random field samples. Owing to a subtle issue of the boundary conditions involved in the corresponding test, we present the corresponding results in an appendix at the end of this paper. For the time being, it suffices to make a note that our ansatz for studying iso-density con-

tours and their morphology works exceedingly well both for simply connected as well as multiply connected surfaces and on Gaussian random fields.

In the next section, we apply SURFGN to cosmological N-body simulations and give an example of the study of the morphology in three models of structure formation: Λ CDM, τ CDM and SCDM.

5 APPLICATIONS: MORPHOLOGY OF THE VIRGO SIMULATIONS

As a first application of the SURFGN code, we report here a morphological study of cosmological simulations. We use dark matter distributions of three cosmological models simulated by the Virgo consortium. The models are (1) a flat model with $\Omega_0 = 0.3$ (Λ CDM), and two models with $\Omega = 1$, namely (2) one with the standard CDM power spectrum (SCDM) and (3) a flat model with the same power spectrum as the $\Omega_0 = 0.3$ Λ CDM model (also referred to as τ CDM). The shape parameter Γ ($=\Omega_0 h$) for SCDM is 0.5, whereas for the other two models $\Gamma = 0.21$. Amplitude of the power spectrum in all models is set so as to reproduce the observed abundance of rich galaxy clusters at the present epoch. A detailed discussion of the cosmological parameters and simulations can be found in Jenkins et al. (1998).

The data consist of 256^3 particles in a box of size $239.5 h^{-1}\text{Mpc}$. In order to carry out a detailed morphological study, we first need to smooth the data and recover the underlying density field. The issue of density field reconstruction has been well explored by several groups studying the topology of the large scale structure. Here we follow the smoothing technique used by Springel et al. (1998) which they adopted for their preliminary topological analysis of the Virgo simulations. We fit a 128^3 grid on to the box.

⁶ It should be noted that the definition of the third Shapefinder L is modified from that reported in Sahni, Sathyaprakash & Shandarin (1998). New definition of L is as given in Eq.9. The newly adopted definition of L incorporates treatment of simply connected and multiply connected surfaces in within a single scheme.

Thus, the size of each cell is $1.875 h^{-1}\text{Mpc}$. Since there are on an average 8 particles per cell, the smoothing is not too sensitive to shot-noise. The samples are fairly rich and we can smooth the fields in two steps. In the first, we apply a Cloud in Cell (CIC) smoothing technique to construct a density field on the grid. Next we smooth this field with a Gaussian kernel which offers us an extra smoothing length-scale. There are various criteria to fix this smoothing scale which depend on the relative sparseness/richness of the samples. To avoid discreteness effect (so that there are no regions in the survey where density is undefined), the simplest criteria for sparse samples has been to set $\lambda \geq 2.5\ell_g$, where ℓ_g is the grid-size. There are other sophisticated criteria to deal with sparse samples which are tested and reported in literature, which need not be reiterated here on account of our samples being rich. We are left with two choices; either to smooth the fields at a scale comparable to r_0 , the correlation scale, or to probe the morphology at smaller length scales with an interest to study the regularity in the behaviour of the MFs; of which the latter is more promising. The average interparticle distance in the present case is $\sim 0.94 h^{-1}\text{Mpc}$, which is far outweighed by the grid-size and the correlation length. Hence, we adopt a modest scale of smoothing, $\lambda = 2 h^{-1}\text{Mpc}$, which is small compared to usual standards as well as enough to provide the necessary smoothing. The Gaussian kernel for smoothing that we adopt here is ⁷

$$W(r) = \frac{1}{\pi^{\frac{3}{2}}\lambda^3} \exp\left(-\frac{r^2}{\lambda^2}\right). \quad (15)$$

In this section we first study the global MFs for all the three models. Next we investigate the morphology of the percolating supercluster network. This is followed by a statistical study of the morphology of smaller structures. We summarize our results in the next section.

5.1 Global Minkowski Functionals

We scan the density fields at 100 values of the density threshold ρ_{TH} , all equispaced in the filling factor

$$FF_V = \int \Theta(\rho - \rho_{\text{TH}}) d^3x, \quad (16)$$

where $\Theta(x)$ is the Heaviside Theta function. FF_V measures the volume-fraction in regions which satisfy the ‘cluster’ criterion $\rho_{\text{cluster}} \geq \rho_{\text{TH}}$ at a given density threshold ρ_{TH} . In the following, we use FF_V as a parameter to label the density contours.

⁷ Since the Gaussian kernel that we use is radially symmetric, it could, in principle, diminish the true extent of anisotropy in filaments and pancakes. This effect could be minimized by considering anisotropic kernels and/or smoothing techniques based on the wavelet transform. An even more ambitious approach is to reconstruct density fields using Delaunay tessellations (van de Weygaert 2002). Density fields reconstructed in this manner appear to preserve anisotropic features and may therefore have some advantage over conventional ‘cloud-in-cell’ techniques followed by an isotropic smoothing (Schaap & Weygaert 2000). Thus, as far as the goal is to utilize the geometry of the patterns to discriminate between the models, such smoothing schemes should prove more powerful. We hope to return to these issues in forthcoming paper(s).

At each level of the density field (labelled by FF_V), we construct a catalogue of clusters (overdense regions) based on a Friends of Friends (FOF) algorithm.⁸ Next we (i) run the SURFGEN code on each of these clusters to model surfaces for each of them and (ii) determine the Minkowski Functionals (MFs) for all clusters at the given threshold (these are referred to in the literature as partial MFs). Global MFs are partial MFs summed over all clusters. Thus, at each level of the density, we first compute the partial MFs and then the global MFs. Our plots of global MFs as functions of FF_V are shown in Figures 13. This figure shows some interesting features. The three cosmological models have appreciably different morphology and hence can be distinguished from one another on the basis of morphological measures. Similarly to the percolation statistic (Dominik & Shandarin 1992) the difference between models is brought out much better if, instead of plotting the MFs against the volume fraction (equivalently ‘volume filling factor’), we choose the ‘mass fraction’ defined as $FF_M = M_{\text{total}}^{-1} \int \rho (\geq \rho_{\text{TH}}) dV$. (The ‘mass fraction’ can be thought of as the ‘volume or mass filling factor’⁹ in (initial) Lagrangian space, while the ‘volume fraction’ is the filling factor in (final) Eulerian space.) By employing this parameter for studying the global MFs, we essentially probe the morphology of the iso-density contours (which may refer to different thresholds of density or density contrast, but) which enclose the same fraction of the total mass. Since clustering tends to pack up the mass into progressively smaller regions of space, such a study connects to aspects of gravitational clustering in a direct way. Thus, we see that at all the values of FF_M the volume that encloses the same fraction of the total mass is least for ΛCDM and most for τCDM . A further advantage of employing this parameter is that the behaviour of the rest of the global MFs is no longer restricted to follow the same pattern (like it is in case of studying global MFs with the volume filling factor as the labelling parameter). Thus, not only the peak, but also the peak-position and the shape of the MF-curves are sensitive to the models being investigated. Thus, the mass fraction parametrisation could be more useful in discriminating the models from one another as well as comparing the models with the observations. Before we commence our analysis of individual objects (connected overdense/underdense regions) we would like to draw the attention of the reader to an issue in nomenclature. The ‘clusters’ and ‘superclusters’ referred to further in this paper are elements constituting the ‘cosmic-web’ and defined on the basis of isodensity contours in N-body simulations. They should not be mistaken for the clusters and superclusters of galaxies seen in the sky.

⁸ The clusters/superclusters discussed in the present paper are defined as connected overdense regions lying above a prescribed density threshold. Due to the large smoothing scale adopted, the overdensity in clusters ranges from $\delta \sim 1$ to $\delta \sim 10$, which makes them more extended (\gtrsim few Mpc) and less dense than the galaxy clusters in (for instance) the Abell catalogue.

⁹ Since the density in the Lagrangian space is uniform there is no difference between the volume and mass fractions.

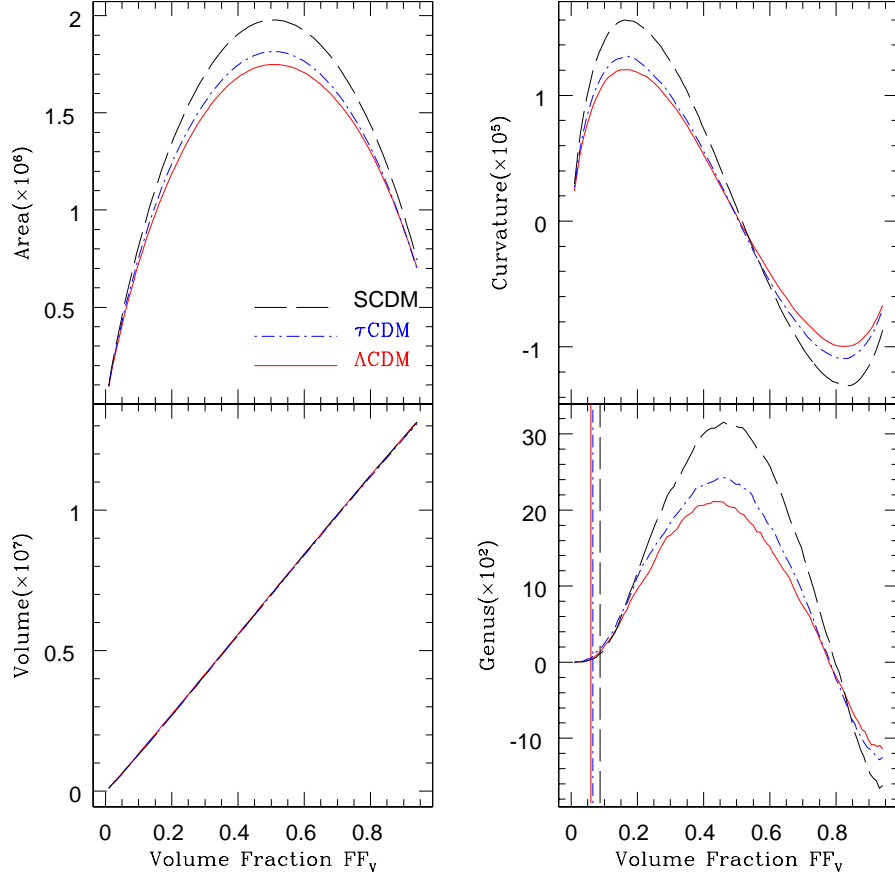


Figure 13. Global Minkowski functionals for Λ CDM, τ CDM and SCDM are shown as functions of the volume fraction (\equiv volume filling factor, FF_V). The volume-curve is the same for all models and grows linearly with the volume fraction; this is simply a restatement of the definition of ‘filling factor’. Notice that the amplitude of the remaining three MFs (Area, Curvature and Genus) is substantially greater in SCDM than in Λ CDM; with τ CDM falling between the two. This could mean that large scale structure is much more ‘spongy’ in SCDM with percolating structures in this model showing many more ‘holes’ (or tunnels) and resulting in a large value for the genus. A relative shift towards left, of the position of the peak of the genus curve in Λ CDM from $FF_V = 0.5$ is indicative of the bubble shift, implying more amount of clumpiness in this model compared to other two models. It should be noted that for a Gaussian random field, the peak occurs at $FF_V = 0.5$. Gravitational clustering modulates the genus curve by lowering its peak and producing a shift to the left (the ‘bubble shift’) or to right (the ‘meatball shift’) depending upon the other model parameters. The relatively large value of the surface area and the curvature may indicate that moderately overdense superclusters have many more ‘twists and turns’ in SCDM than in either τ CDM or Λ CDM, at identical values of the filling factor. In all models the genus curve has a large negative value at large values of the volume fraction. The reason for this is that the percolating supercluster, at extremely low density thresholds (high FF_V), occupies most of the volume. Voids exist as small isolated bubbles in this vast supercluster and lead to a large negative genus whose value is of the same order as the total number of voids. In the opposite case, at very high density thresholds associated with small filling fractions, we probe the morphology of isolated and simply connected clusters. Since the genus for these clusters vanishes, the global topology of large scale structure at high thresholds of the density generically approaches zero for all the models. The vertical lines in the lower right panel show the percolation threshold in SCDM (dashed), τ CDM (dot-dashed), and Λ CDM (solid) which occurs at intermediate density thresholds corresponding to density contrast $\delta \sim 1$. It is clear from this figure that the percolating supercluster has a relatively simple topology at the onset of percolation. The rapid increase in genus value as one moves to lower density thresholds (larger FF_V) reflects the progressive increase in the ‘sponge-like’ topology of the percolating supercluster which is more marked in SCDM than in Λ CDM.

5.2 Cluster abundance and percolation

In this subsection we first discuss the percolation properties of the three density fields being studied. In this context we study how the total number of clusters and the fractional volume in the largest cluster vary as we scan through a set of density levels corresponding to equispaced fractions of volume and total mass. Figure 15 shows the volume fraction and mass fraction as a function of the density contrast. It is

interesting to note that SCDM and τ CDM show the same pattern of behaviour which differs from Λ CDM. It is further to note that at high density thresholds ($\delta \gtrsim 1$) the filling factor (at a constant density threshold) is greater in Λ CDM than in SCDM or τ CDM, while exactly the reverse is true for underdense regions. This figure, which relates $FF_{M,V}$ to δ , serves as a reference point to all of our subsequent percolation studies. Figure 15 also shows that, relative to

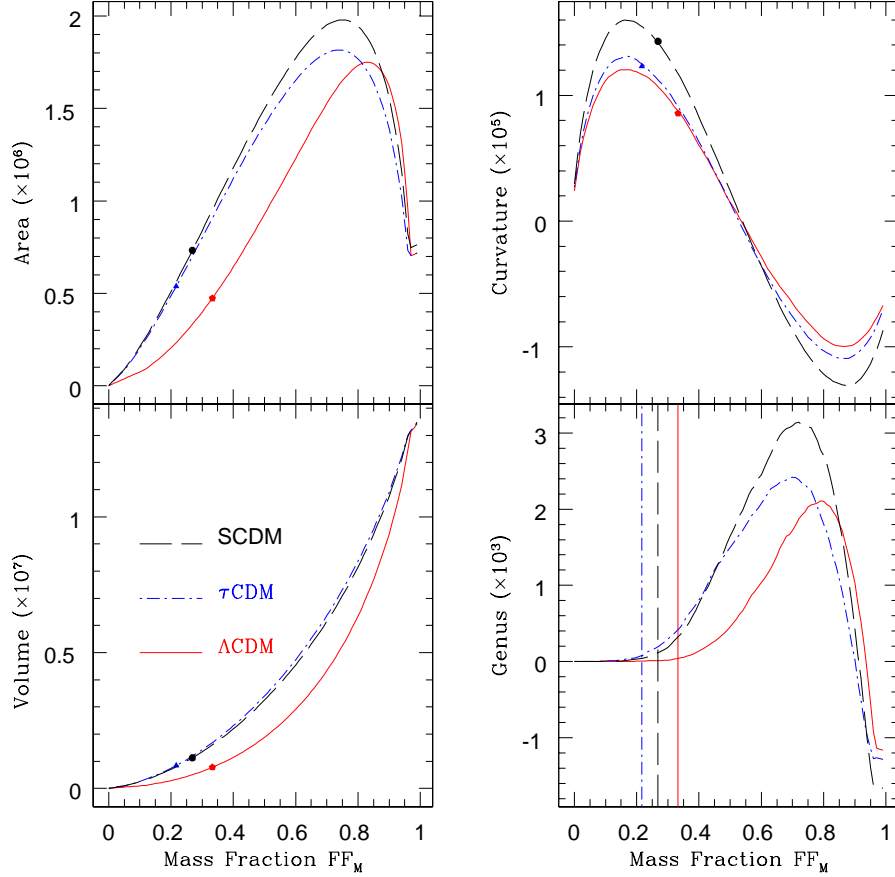


Figure 14. Global Minkowski functionals for Λ CDM, τ CDM and SCDM are shown as functions of the mass fraction defined as $FF_M = M_{\text{total}}^{-1} \int \rho (\geq \rho_{\text{TH}}) dV$. We see that some of the degeneracy between the different models seen in Fig. 13 is broken when one plots the MFs in terms of the mass fraction FF_M instead of the volume fraction FF_V . The markers on the three curves show the mass fraction at the onset of percolation in each of the three cosmological models. (For the sake of greater clarity, vertical lines through the markers are shown in the lower right panel.)

other models, *more mass occupies less space in Λ CDM*. Thus almost 67% of the total mass in the Λ CDM universe resides in just 25% of the volume. (In case of τ CDM and SCDM $\sim 62\%$ mass occupies $\sim 34\%$ volume.)

A statistical pair which help quantify the geometry of large scale structure and its morphology are the ‘Number of Clusters Statistic’ (NCS) and the ‘Largest Cluster Statistic’ (LCS); both are shown in Figure 16. The Number of Clusters Statistic shows cluster abundance as a function of the density contrast (lower left), mass fraction (lower middle) and volume fraction (lower right). The Largest Cluster Statistic measures the fractional cluster volume occupied by the largest cluster:

$$LCS = \frac{V_{\text{LC}}}{\sum_i V_i}, \quad (17)$$

where V_i is the volume of the i -th cluster in the sample and V_{LC} is the volume occupied by the largest cluster. Summation is over all clusters evaluated at a given threshold of the density and includes the largest cluster. In Figure 16 LCS is shown as a function of the density contrast (upper left),

mass fraction (upper middle) and volume fraction (upper right).

The square, triangle and circle in NCS denote critical values of the parameters $\delta = \delta_{\text{cluster-max}}$, $FF_V = FF_{\text{cluster-max}}$ and FF_M at which the cluster abundance peaks in a give model. Similar etchings on the LCS curves denote values of $\delta = \delta_{\text{perc}}$, $FF_V = FF_{\text{perc}}$ and FF_M at which the largest cluster first spans across the box in at least one direction. This is commonly referred to as the ‘percolation threshold’. It is important to note that the number of clusters in SCDM is considerably greater than the number of clusters in Λ CDM at most density thresholds. It is also interesting that percolation takes place at higher values of the density contrast (and correspondingly lower values of the volume filling factor) in the case of Λ CDM. ($\delta_{\text{perc}} \simeq 2.3$ for Λ CDM, $\delta_{\text{perc}} \simeq 1$ for SCDM and τ CDM.) Furthermore, while in the case of Λ CDM $\delta_{\text{cluster-max}} \geq \delta_{\text{perc}}$, in the case of SCDM and τ CDM, $\delta_{\text{cluster-max}} \lesssim \delta_{\text{perc}}$. Thus in the latter two models, as the density threshold is lowered, the cluster abundance initially peaks, then, as the threshold is lowered further, neighboring clusters merge to form the percolating supercluster. In Λ CDM on the other hand, the threshold at

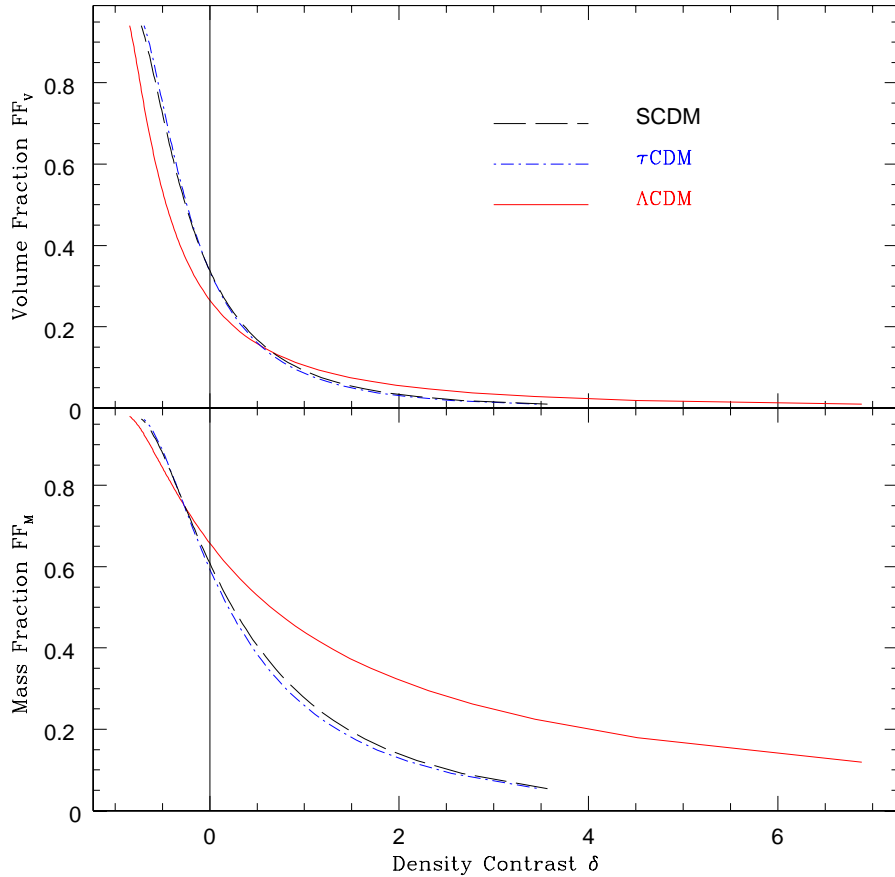


Figure 15. Here we study the evolution of the volume fraction and the mass fraction w.r.t. the density contrast for all the three models. Λ CDM shows maximum density contrast. SCDM and τ CDM form another class of models which have similar density contrasts but smaller than Λ CDM. The vertical line across both the panels refers to the mean density, which can be used as a marker to study the mass fraction which is contained in the overdense volume (the volume occupied by regions above the mean density). We note that the overdense volume in Λ CDM is $\sim 25\%$ which is about 10% smaller than that occupied by the other two models. At the same time, the mass that this volume encloses is $\sim 67\%$ and is about 5% larger than that enclosed by the overdense volume in the other two models.

which the cluster abundance peaks also signals the formation of the percolating supercluster. Having said this we would like to add a word of caution: the analysis of one realization alone does not allow us to assess reliably the statistical fluctuations in the threshold of percolation. Therefore the final conclusion can be drawn only after a study of many realizations of each model.

Clearly both the LCS threshold δ_{perc} and the NCS threshold $\delta_{\text{cluster-max}}$ contain important information and most of our subsequent description of supercluster morphology will be carried out at one of these two thresholds. Table 3 shows the Minkowski functionals and associated Shapefinders for the 10 largest (most voluminous) superclusters compiled at the percolation threshold for the three cosmological models Λ CDM, τ CDM and SCDM while Table 3 lists values for the Planarity and Filamentarity for these superclusters along with the mass that these enclose and their genus value.

Our $(239.5h^{-1}\text{Mpc})^3$ Λ CDM universe contains 1334 clusters & superclusters at the percolation threshold. Of these the smallest is quasi-spherical with a radius of a few Megaparsec while the largest is extremely filamentary and

percolates through the entire simulation box (see figure 17). From Figures 17 & 16 we find that the percolating Λ CDM supercluster is a slim but massive object.¹⁰ It contains 4.5% of the total mass in the universe yet occupies only 0.6% of the total volume. In SCDM the percolating supercluster contains 4.4% of the total mass and occupies 1.2% of the total volume, i.e., a similar mass occupies two times greater volume than in the Λ CDM. The $\sim 10^3$ Λ CDM clusters with $\delta \geq \delta_{\text{perc}}$ occupy 4.4% of the total volume and contain 33% of the total mass in the universe. Gravitational clustering thus ensures that most of the mass in the Λ CDM universe is distributed in coherent filamentary regions which occupy very little volume but contain much of the mass. (Of the

¹⁰ Surface visualization is a difficult task especially if we wish to follow tunnels through superclusters to check whether our visual impression of the genus agrees with that calculated using the Euler formula (8). MATLAB has been used for surface plotting and the ‘reality’ of tunnels is ascertained by rotating surfaces and by viewing the supercluster at various angles.

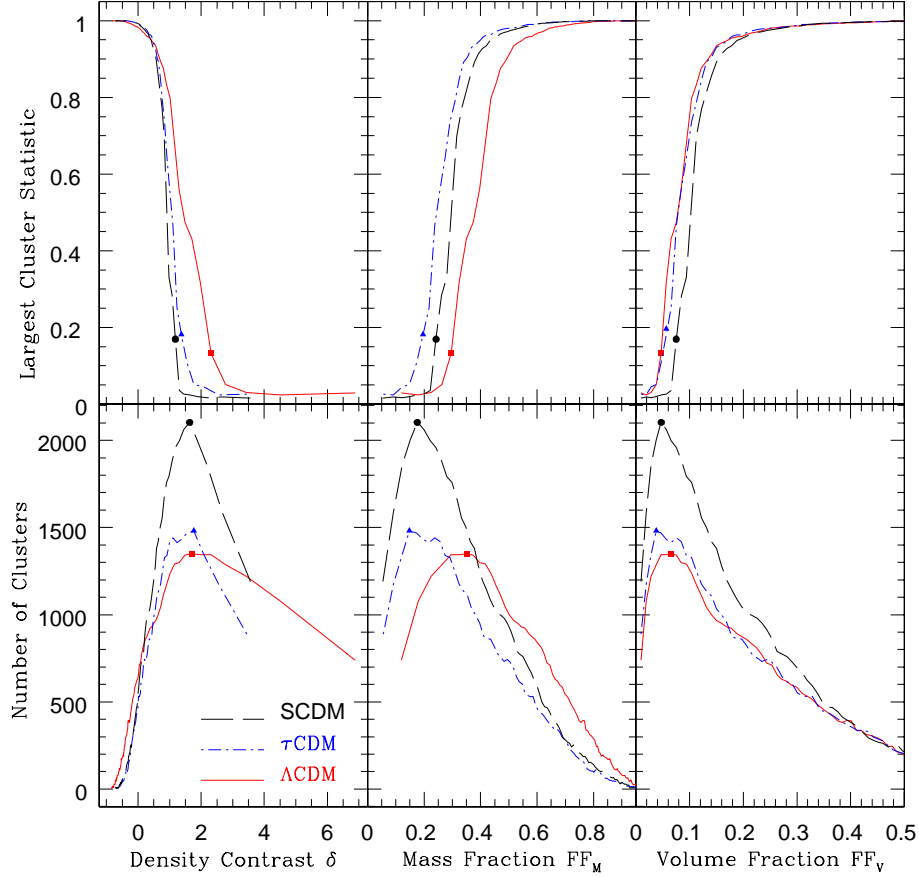


Figure 16. Number of Clusters statistic (NCS) and the Largest Cluster Statistic (LCS) are studied as functions of the density contrast δ (left panels), mass fraction FF_M (middle panels) and volume fraction, (equivalently volume filling factor), FF_V (right panels). The markers on the three curves, in the case of NCS, show values of $\delta_{\text{cluster-max}}$ (left), $FF_{M,\text{max}}$ (middle) and $FF_{V,\text{max}}$ (right) at which the cluster abundance peaks. In the case of LCS, the markers indicate percolation values of δ_{perc} (left), $FF_{M,\text{perc}}$ (middle) and $FF_{V,\text{perc}}$ (right) at which the largest cluster percolates by running through the entire simulation box.

1334 Λ CDM clusters and superclusters identified at the percolation threshold, the ten most voluminous are extremely filamentary and contain close to 40% of the total cluster mass (see table 3). The remaining 60% of the mass is distributed amongst other 1324 objects !)

The percolating supercluster is more filamentary and less planar in Λ CDM [$(P, F)_{\Lambda\text{CDM}} = (0.13, 0.81)$] than in SCDM [$(P, F)_{\text{SCDM}} = (0.14, 0.78)$]. The percolating supercluster of the τ CDM is least filamentary and most planar with $(P, F)_{\tau\text{CDM}} = (0.15, 0.70)$. It is interesting that superclusters evaluated at δ_{perc} are more ‘porous’ (*i.e.* have a larger genus) in SCDM than their counterparts in Λ CDM. For instance the percolating supercluster in Λ CDM has only 6 ‘holes’ which tunnel all the way through it, while 20 tunnels pass through the percolating supercluster in SCDM; see Table 3. (This number increases as the density threshold is lowered as demonstrated in Figure 18.) Another interesting feature of gravitational clustering appears to be that although the volume occupied by clusters at $\delta_{\text{cluster-max}}$ does not vary much between models, the fractional mass contained in Λ CDM clusters is *almost twice* that in either τ CDM or SCDM; see Figure 16.

5.3 Cluster Morphology

Cosmic density fields contain a wealth of information. As demonstrated in Fig. 16, at density thresholds significantly lower than δ_{perc} most clusters merge to form a single percolating supercluster. On the other hand, the slightly larger NCS density contrast, $\delta_{\text{cluster-max}}$, provides an excellent threshold at which to study the morphology of individual objects since it is precisely at $\delta_{\text{cluster-max}}$ that the cluster abundance peaks. We study the morphology and topology of large scale structure in a two-fold manner: (i) properties of all superclusters are analysed at one of the two thresholds: $\delta_{\text{perc}}, \delta_{\text{cluster-max}}$; (ii) the morphology of the largest supercluster is extensively probed as a function of the density contrast.

Figure 18 shows the evolution of the morphology and topology of the largest cluster as we scan through different threshold levels of the Λ CDM density field. The density contrast, volume fraction and genus for a few of these levels have been labelled and are given in the right corner of the figure. We note that at high density thresholds the largest cluster occupies a very small fraction of the total volume and its

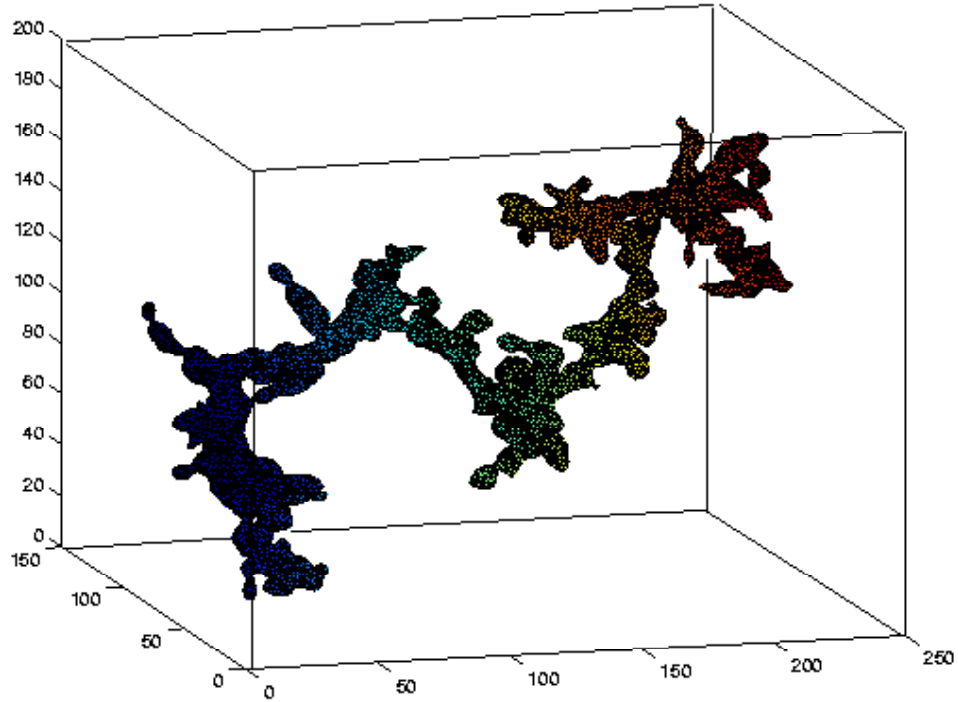


Figure 17. The largest (percolating) supercluster in Λ CDM. This cluster is selected at the density threshold which marks the onset of percolation ($\delta_{\text{perc}} = 2.3$). As demonstrated in the figure, the cluster at this threshold percolates through the entire length of the simulation box. It is important to note that the percolating supercluster occupies only a small fraction of the total volume and its volume fraction (filling factor) is only 0.6%. Our percolating supercluster is a multiply connected and highly filamentary object. Its visual appearance is accurately reflected in the value of the Shapefinder diagnostic assigned to this supercluster: $(T, B, L) = (5.63, 7.30, 70.03) h^{-1}\text{Mpc}$ and $(P, F, G) = (0.13, 0.81, 6)$.

shape is characterized by significant filamentarity (~ 0.67) and negligible planarity (~ 0). We note a sharp increase in the filamentarity of the largest cluster as we approach the percolation threshold (shown in the figure as a solid triangle). At smaller values of the density contrast, $\delta \lesssim 3$, supercluster filamentarity rapidly drops while its planarity considerably increases. The drop in filamentarity of the supercluster is accompanied by a growth in its complexity with the result that, at moderately low thresholds ($\delta \sim 0.5$), the percolating supercluster can contain several hundred tunnels. At very low thresholds ($\delta \lesssim 0.5$) the percolating supercluster is an isotropic object possessing negligible values of both planarity (P) and filamentarity (F).

Since δ_{perc} and $\delta_{\text{cluster-max}}$ contain information pertaining to morphology and connectivity, we compile partial MFs for individual clusters at both these thresholds for the three cosmological models Λ CDM, SCDM and τ CDM. We find it convenient to work with the cumulative probability function (CPF) which we define as the normalized count of clusters with the value of a quantity Q to be greater than q at a given value 'q'. The quantity Q could be one of the MFs or one of the Shapefinders. We shall study the dependence of CPF with Q on a log-log scale.

Our results are presented in Figures 19, and 20 for clusters compiled at the NCS threshold $\delta_{\text{cluster-max}}$. For large values of the Minkowski functionals (V, A, C) the CPF declines rapidly. Although the curves may look similar, some of them are statistically very different from their peers. The first four columns of Table 4 show the results of the

Kolmogorov-Smirnov test applied to the distribution of the MFs. (We do not carry out a similar exercise for the genus since the vast majority of clusters at the NCS threshold are simply connected.) In particular the CPF of the masses clearly distinguish the Λ CDM model from SCDM & τ CDM, in agreement with Fig. 19.

Figure 20 shows the Cumulative Probability Function for planarity and filamentarity in our cluster sample. The last two columns of Table 4 show the results of the KS test for these statistics. For all three pairs they are among three best discriminators of the models. The value of KS statistic d suggests that the signal comes from relatively small values of P (< 0.1) and F (< 0.25). The more conspicuous differences in the tail of the distribution is not statistically significant due to poor statistics. Clusters in Λ CDM are the least anisotropic, a fact which corresponds to their relatively early formation and therefore longer evolution. From Figure 20 we also find that clusters at the NCS threshold are significantly more filamentary than they are planar. This appears to be a generic prediction of gravitational clustering as demonstrated by Arnol'd, Shandarin & Zel'dovich (1982); Klypin & Shandarin (1983); Sathyaprakash, Sahni & Shandarin (1996) and Bond, Kofman & Pogosyan (1996).

Figure 21 is a scatter plot of Shapefinders T, B, L for clusters in Λ CDM defined at the percolation threshold. The strong correlation between T and B in the left panel indicates that two (of three) dimensions defining any given cluster assume similar values and are of the same order as

Table 3. The ten most voluminous superclusters (determined at the percolation threshold) are listed with the mass they enclose, their associated Minkowski functionals (Volume, area, curvature and genus) and Shapefinders T, B, L, P and F . The first row in each cosmological model describes the percolating supercluster and appears in boldface. It is interesting that in all three cosmological models the top ten superclusters contain roughly 40% of the total mass in overdense regions with $\delta \geq \delta_{\text{perc}}$. (The precise numbers are 40% for Λ CDM, 37.8% for SCDM and 45.6% in τ CDM.) It should also be noted that the mass of a typical supercluster in Λ CDM is somewhat smaller than that in the other two models mainly on account of the fact that the adopted particle mass in Λ CDM simulations is smaller than in simulations of SCDM and τ CDM. (The particle mass in Λ CDM is $6.86 \times 10^{10} h^{-1} M_{\odot}$ and that in SCDM and τ CDM is $2.27 \times 10^{11} h^{-1} M_{\odot}$ (Jenkins et al. 1998)). It should be noted that the interpretation of L as the ‘linear length’ of a supercluster can be misleading for the case of superclusters having a large genus. In this case $L \times (G + 1)$ provides a more realistic estimate of supercluster length since it allows for its numerous twists and turns. The morphology of the objects is conveyed through their planarity P and filamentarity F . We note that the most voluminous and massive structures are highly filamentary in all the models. The largest supercluster is most filamentary in case of Λ CDM and least so in case of τ CDM.

Model	Mass (M/M_{\odot})	Volume ($h^{-1} \text{Mpc}$) ³	Area ($h^{-1} \text{Mpc}$) ²	Curvature $h^{-1} \text{Mpc}$	Genus	Shapefinders				
						T ($h^{-1} \text{Mpc}$)	B ($h^{-1} \text{Mpc}$)	L ($h^{-1} \text{Mpc}$)	P	F
Λ CDM $\delta = 2.31$	5.17×10^{16}	8.45×10^4	4.5×10^4	6.16×10^3	6	5.63	7.30	70.03	0.13	0.81
	1.87×10^{16}	3.21×10^4	1.7×10^4	2.33×10^3	1	5.63	7.34	92.74	0.13	0.85
	1.30×10^{16}	2.22×10^4	1.22×10^4	1.76×10^3	1	5.47	6.93	70.00	0.12	0.82
	1.41×10^{16}	2.13×10^4	1.02×10^4	1.29×10^3	0	6.27	7.90	102.7	0.12	0.86
	7.68×10^{15}	1.21×10^4	6.35×10^3	8.78×10^2	0	5.71	7.22	69.95	0.12	0.81
	6.75×10^{15}	1.19×10^4	6.82×10^3	1.02×10^3	1	5.25	6.70	40.53	0.12	0.72
	5.85×10^{15}	1.08×10^4	6.12×10^3	9.16×10^2	0	5.3	6.68	72.90	0.11	0.83
	7.13×10^{15}	1.01×10^4	5.46×10^3	8.19×10^2	0	5.57	6.65	65.24	0.09	0.81
	5.19×10^{15}	8.6×10^3	4.74×10^3	7.07×10^2	0	5.44	7.00	56.33	0.10	0.79
	5.04×10^{15}	8.1×10^3	4.25×10^3	5.71×10^2	1	5.72	7.44	22.74	0.13	0.51
τ CDM $\delta = 1.37$	1.45×10^{17}	1.37×10^5	7.57×10^4	1.03×10^4	19	5.42	7.36	40.94	0.15	0.70
	4.04×10^{16}	3.97×10^4	2.35×10^4	3.58×10^3	2	5.07	6.57	94.93	0.13	0.87
	3.16×10^{16}	2.98×10^4	1.72×10^4	2.48×10^3	1	5.20	6.94	98.53	0.14	0.87
	2.45×10^{16}	2.27×10^4	1.32×10^4	1.97×10^3	1	5.16	6.71	78.47	0.13	0.84
	1.99×10^{16}	1.77×10^4	9.38×10^3	1.29×10^3	1	5.66	7.26	51.44	0.12	0.75
	1.65×10^{16}	1.63×10^4	9.35×10^3	1.31×10^3	2	5.24	7.14	34.73	0.15	0.66
	1.74×10^{16}	1.39×10^4	6.69×10^3	8.14×10^2	3	6.26	8.22	16.20	0.14	0.33
	1.55×10^{16}	1.38×10^4	8.06×10^3	1.12×10^3	1	5.13	7.21	44.45	0.17	0.72
	1.46×10^{16}	1.34×10^4	7.8×10^3	1.16×10^3	2	5.15	6.72	30.77	0.13	0.64
	1.48×10^{16}	1.32×10^4	7.32×10^3	1.04×10^3	2	5.42	7.01	27.68	0.13	0.60
SCDM $\delta = 1.19$	1.66×10^{17}	1.7×10^5	9.89×10^4	1.44×10^4	20	5.14	6.88	54.57	0.14	0.78
	4.15×10^{16}	4.24×10^4	2.6×10^4	4.07×10^3	2	4.90	6.38	107.94	0.13	0.89
	3.43×10^{16}	3.52×10^4	2.04×10^4	2.93×10^3	3	5.19	6.96	58.27	0.15	0.79
	2.02×10^{16}	1.95×10^4	1.07×10^4	1.48×10^3	3	5.47	7.21	29.47	0.14	0.61
	1.85×10^{16}	1.94×10^4	1.12×10^4	1.56×10^3	2	5.19	7.08	42.05	0.15	0.71
	1.61×10^{16}	1.6×10^4	9.64×10^3	1.39×10^3	3	4.97	6.95	27.58	0.17	0.60
	1.34×10^{16}	1.36×10^4	7.59×10^3	1.08×10^3	2	5.37	7.05	28.59	0.14	0.60
	1.30×10^{16}	1.34×10^4	8.07×10^3	1.25×10^3	2	4.97	6.47	33.07	0.13	0.67
	1.29×10^{16}	1.25×10^4	7.11×10^3	9.98×10^2	2	5.27	7.12	26.50	0.15	0.58
	1.30×10^{16}	1.21×10^4	6.87×10^3	9.88×10^2	2	5.27	6.95	26.22	0.14	0.58

the correlation length. (Note that $T \simeq B \simeq 5h^{-1}$ Mpc for the largest superclusters in Table 3.) The clustering of objects near $T \simeq B$ ($P \simeq 0$) in this panel suggests that our clusters/superclusters are either quasi-spherical or filamentary. The scatter plot between B & L in the right panel of Figure 21 breaks the degeneracy between spheres and filaments. The mass-dependence of morphology is highlighted in this panel in which larger dots denote more massive objects. This figure clearly reveals that more massive clusters/superclusters are, as a rule, also more filamentary, while smaller, less massive objects, are more nearly spherical. The concentration of points near the ‘edge’ of the scatter plot in the right panel, arises due to an abundance of low mass

compact quasi-spherical objects with $L \simeq B$ ($F \simeq 0$). The large number of massive superclusters with $F > 0.5$ serves to highlight the important fact that the larger and more massive elements of the supercluster chain consist of highly elongated filaments as much as $\sim 100h^{-1}$ Mpc in length, with mean diameter $\sim 5h^{-1}$ Mpc (see Table 3). It is important to reiterate that almost 40% of the total overdense mass resides in the ten largest objects listed in table 3, while the remaining 60% is distributed among 1324 clusters.

We also find short filaments to be generally thinner than longer ones in agreement with predictions made by the adhesion model with regard to the formation of hierar-

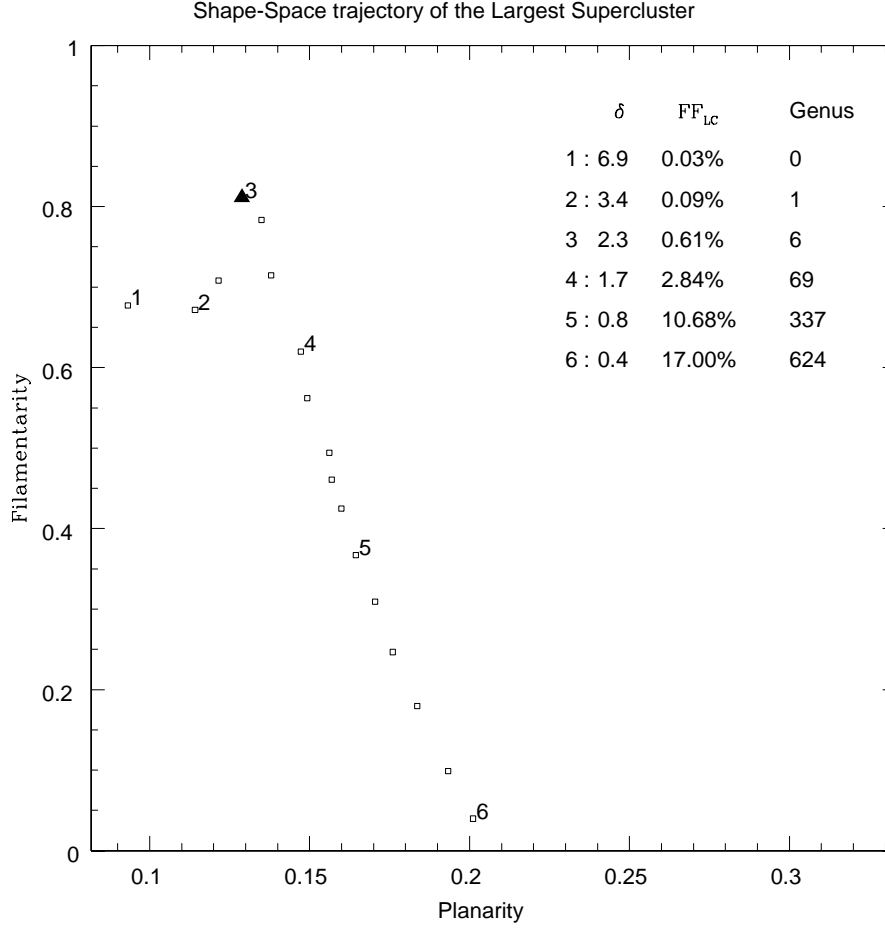


Figure 18. The morphological evolution of the largest supercluster in Λ CDM is shown as a series of open squares in shape-space $\{F, P\}$. Each square corresponds to a different value of the density threshold which is progressively lowered from a large initial value ($\delta \simeq 6.9$; left most square) until the mean density level ($\delta = 0$; lower most square). The legend lists the density contrast, the associated volume fraction and the genus of the largest supercluster at six monotonically decreasing values of the density contrast ($1 \rightarrow 6$). At the highest ($\delta \simeq 6.9$), the largest cluster appears to have a large filamentarity and a small planarity. The solid triangle (labelled 3) refers to the percolation threshold at which the largest cluster first spans across the simulation box. After percolation, the filamentarity rapidly decreases from a maximum value of 0.81 to 0.0 as the threshold is lowered from $\delta \simeq 2$ to $\delta \simeq 0$. The decline in filamentarity of the largest cluster is accompanied by growth in its complexity as revealed by its genus value, e.g., the fractional volume occupied by the largest cluster at the mean density is $\sim 26\%$ and its genus exceeds a thousand.

Table 4. The Kolmogorov-Smirnov statistic d (first row for each pair of models) and the probability (second row) that the two data sets are drawn from the same distribution. The models Λ CDM, τ CDM and SCDM are compared on the basis of three Minkowski functionals: volume (V), area (A), integrated mean curvature (C), as well as mass (M) and the Shapefinders: thickness (T), breadth (B), length (L), planarity (P), and filamentarity (F). Boldface highlights the three *smallest probabilities* for each pair of models.

Models	M	V	A	C	T	B	L	P	F
Λ CDM - τ CDM	0.093	0.067	0.059	0.037	0.082	0.070	0.037	0.15	0.101
	9.4×10^{-4}	0.036	0.094	0.56	5.0×10^{-3}	0.026	0.56	6.5×10^{-9}	2.2×10^{-4}
Λ CDM - SCDM	0.077	0.060	0.057	0.049	0.079	0.067	0.049	0.12	0.074
	4.6×10^{-3}	0.048	0.069	0.17	2.9×10^{-3}	0.018	0.16	3.2×10^{-7}	6.3×10^{-3}
τ CDM - SCDM	0.034	0.024	0.032	0.041	0.021	0.023	0.042	0.052	0.046
	0.54	0.90	0.61	0.32	0.97	0.92	0.29	0.096	0.19

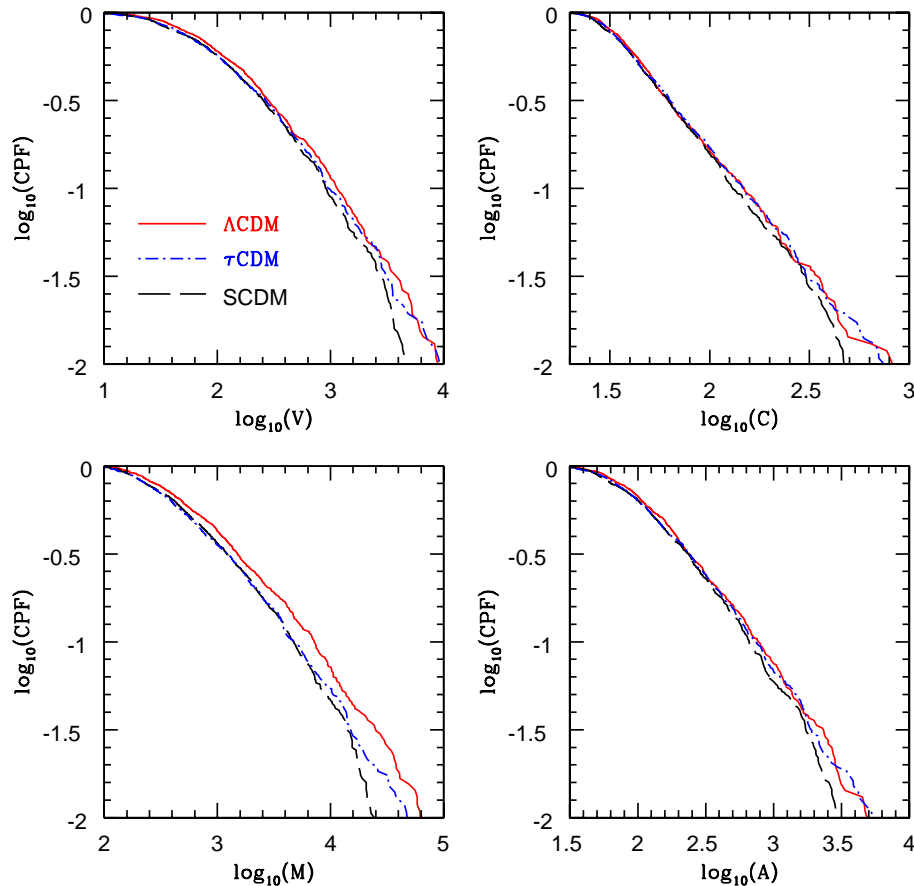


Figure 19. Cumulative Probability Function (CPF) is shown as a function of total mass in superclusters (lower left) and as a function of the three Minkowski functionals volume (V), surface area (A) and mean extrinsic curvature (C). Superclusters are defined to be connected overdense regions lying above the NCS threshold $\delta_{\text{cluster-max}}$. (The cluster abundance peaks at $\delta = \delta_{\text{cluster-max}}$ (see figure 16) which makes this a convenient threshold at which to probe morphology.) The colour type and line type hold the same meaning across all the panels.

chical filamentary structure during gravitational clustering (Kofman, Pogosyan, Shandarin & Melott 1992).

To further probe the morphology of clusters and superclusters we define the notion of shape-space in Figure 22. Shape-space is two dimensional with the planarity (of a cluster) plotted along the x-axis and its filamentarity along the y-axis. (One can also incorporate a third dimension showing the genus.) The first panel in Figure 22 is a scatter plot of P and F for clusters in Λ CDM. The sizes of dots in the middle panel are proportional to cluster mass. We note that the most massive structures are also very filamentary. In the right panel we try to relate the shape of the structures with their topology by scaling the size of the dots with the genus value of clusters having a given morphology (P, F). As shown here, clusters which are multiply connected (larger dots are indicative of more complicated topologies) are also more filamentary. Together, the three panels show us that more massive superclusters are frequently very filamentary and often also topologically quite complex. We also see that a large number of less massive superclusters are simply connected and prolate. These structures are a few Mpc across along

their two shorter dimensions and ~ 20 Mpc along the third, and therefore have appreciable filamentarity ($F \sim 0.3$).

6 DISCUSSION AND CONCLUSIONS

This paper presents a new technique for studying the geometrical and topological properties of large scale structure using the Minkowski functionals (MFs). Given a density field reconstructed by appropriately smoothing a point data set consisting (say) of a distribution of galaxies, our ansatz: (i) constructs closed polyhedral surfaces of constant density corresponding to excursion sets of a density field, using for this purpose a surface generating triangulation scheme (SURFGEN); (ii) SURFGEN evaluates the Minkowski functionals (volume, surface area, extrinsic curvature and genus) thus providing full morphological and topological information of three dimensional iso-density contour surfaces corresponding to a given data set. Evaluated in this manner, the Minkowski functionals can be used to study the properties of individual objects lying either above (clusters, superclusters) or below (voids) a given density threshold. They

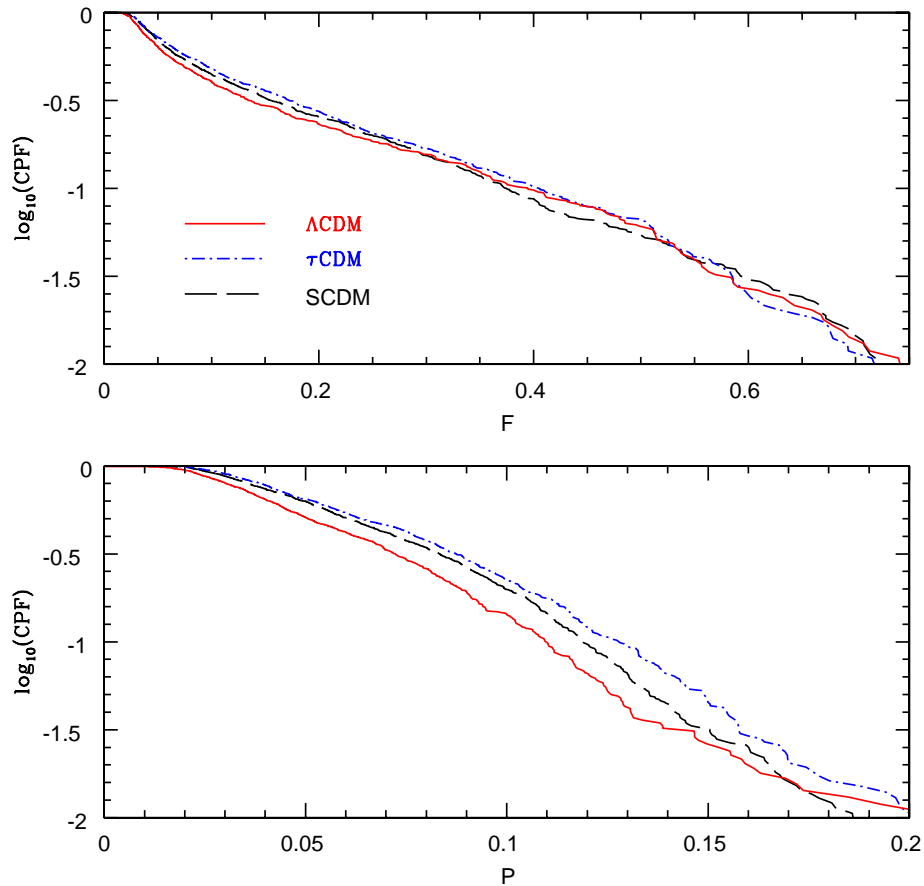


Figure 20. Cumulative Probability Function (CPF) for filamentarity (F) and the planarity (P) of superclusters selected at the density threshold $\delta_{\text{cluster-max}}$. The colour type and line type hold the same meaning for both the panels.

can also be used to study the morphological properties of the full supercluster-void network at (say) the percolation threshold. The ratio's of Minkowski functionals (Shapefinders) are used to probe the shape of iso-density surfaces which sample the distribution of large scale structure at different thresholds of the density. (The highest density thresholds correspond to galaxies and clusters of galaxies, moderate thresholds correspond to superclusters while the lowest density thresholds characterize voids.) The performance of our ansatz has been tested against both simply and multiply connected surfaces such as the sphere, triaxial ellipsoid and triaxial torus. These three eikonal bodies can be smoothly deformed to give surfaces which are spheroidal, pancake-like (oblate) and filament-like (prolate) etc. Analytically known values of the Minkowski functionals for these surfaces allow us to test both our surface modelling scheme and our evaluation of Minkowski functionals from triangulation. Remarkably, we find that volume, area and integrated extrinsic curvature are determined to an accuracy of better than 1% on all length-scales for both simply and multiply connected surfaces. The integrated intrinsic curvature (genus) is evaluated exactly. We also find that SURFGEN is remarkably accurate at calculating the MFs for Gaussian random fields (see the appendix). Having validated the performance of the

code against eikonal surfaces and Gaussian random fields, we apply our method to cosmological simulations of large scale structure performed by the Virgo consortium. We study the geometry and topology of large scale structure in three cosmological scenarios - Λ CDM, τ CDM and SCDM. All three cosmologies are analysed at the present epoch ($z=0$) using global MFs, partial MFs and Shapefinders. (The redshift evolution of geometry and topology will be discussed in a companion paper.) Our main conclusions are summarized below:

- Using the Minkowski functionals we show that, like other diagnostics of clustering, supercluster morphology too is sensitive to the underlying cosmological parameter set characterizing our universe. Although the three cosmological models considered by us, Λ CDM, τ CDM and SCDM display features which are qualitatively similar, the geometrical and morphological properties of these models are sufficiently distinct to permit differentiation using MFs. We demonstrate that studying Minkowski Functionals using mass-parameterization significantly enhances their discriminatory power.
- SURFGEN employs a new contour-based method for determining topology. This method evaluates the genus for an iso-density contour surface directly, by applying the Euler

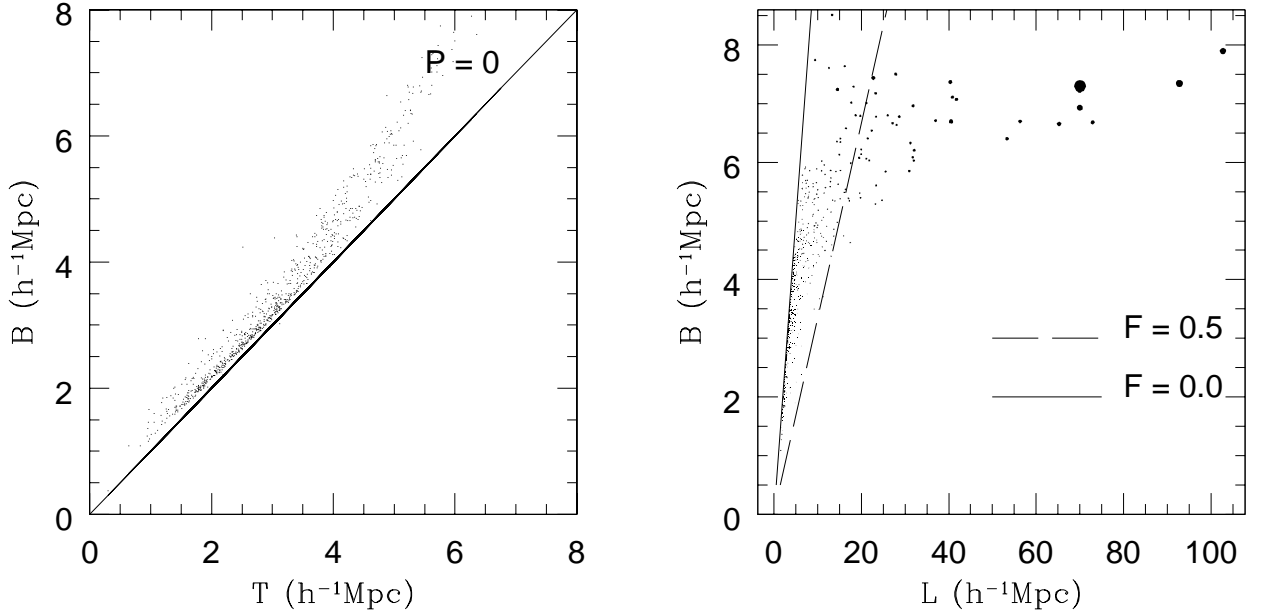


Figure 21. Scatter plot for the pair of Shapefinders T , B (left panel) and B , L (right panel) defining the morphology of clusters/superclusters in the Λ CDM model. The strong correlation between T and B in the left panel near the line $P = 0$ indicates that two of the three dimensions defining a cluster are equal and of the same order as the correlation length (\simeq few Mpc.). Judging from the left panel we find that clusters/superclusters in Λ CDM are either quasi-spherical or filamentary (since both satisfy $T \simeq B \Rightarrow P \simeq 0$). The degeneracy between spheres and filaments is lifted by the right panel which is a mass-weighted scatter plot for the Shapefinders B , L . Each dot in this panel refers to a cluster and its area is proportional to the fraction of mass in that cluster. The concentration of points near the line $F = 0$ ($B = L$) reflects the fact that a large number of smaller clusters are quasi-spherical. The more massive structures, on the other hand, tend to be filamentary and the largest and most massive supercluster has $F = 0.81$. All objects are determined at the percolation threshold.

formula Eq.(8) to the triangulated surface, and presents a significant improvement over earlier grid-based methods of determining topology (Melott 1990).

- A study of percolation and cluster abundance reveals several interesting aspects of the gravitational clustering process. For all models, on decreasing the density threshold to progressively smaller values one reaches the critical percolation threshold at which the largest supercluster runs through (percolates) the simulation box. Percolation is reached at moderate values of the density contrast ranging from $\delta_{\text{perc}} \simeq 2.3$ for Λ CDM to $\delta_{\text{perc}} \simeq 1.2$ for SCDM. The abundance of clusters reaches a maximum value at (or very near) the percolation threshold and the percolating supercluster occupies a rather small amount of space in all three cosmological models. Thus the fraction of total simulation-box volume contained in the percolating supercluster is least in Λ CDM (0.6%) and greatest in SCDM (1.2%). When taken together, all overdense objects at the percolation threshold occupy 4.4% of the total volume in the Λ CDM model. For comparison, the volume fraction in overdense regions at the percolation threshold is $\sim 16\%$ in an idealised, continuous Gaussian random field (Shandarin & Zel'dovich 1989). This fraction can increase upto $\sim 30\%$ for Gaussian fields generated on a grid (Yess & Shandarin 1996; Sahni, Sathyaprakash & Shandarin 1997). The fact that clusters & supercluster occupy a very small fraction of the total volume appears to be a hallmark of the gravitational

clustering process which succeeds in placing a large amount of mass ($\sim 30\%$ of the total, in the case of Λ CDM) in a small region of space ($\sim 4\%$). The low filling fraction of the percolating supercluster in Λ CDM (0.006) strongly suggests that this object is either planar or filamentary (Sahni, Sathyaprakash & Shandarin 1997) and a definitive answer to this issue is provided by the Shapefinder statistic.

- Shapefinders were introduced to quantify the visual impression one has of the supercluster-void network of being a cosmic web of filaments interspersed with large voids (Sahni, Sathyaprakash & Shandarin 1998). By applying the Shapefinder statistics via SURFGEN to realistic N-body simulations we have demonstrated that: (i) Most of the mass in the universe is contained in large superclusters which are also extremely filamentary; the vast abundance of smaller clusters and superclusters tends to be prolate or quasi-spherical. (ii) Of the three cosmological models the percolating supercluster in Λ CDM is the most filamentary ($F \simeq 0.81$) and the supercluster in τ CDM the least ($F \simeq 0.7$). (iii) The percolating supercluster in Λ CDM is topologically a much simpler object than its counterpart in τ CDM, with the former having only $\simeq 6$ tunnels compared to $\simeq 19$ in the latter. Other differences between the models are quantified in Figures 13 – 22. We also show that among various morphological parameters, the Planarity and Filamentarity of clusters and superclusters is one of the most

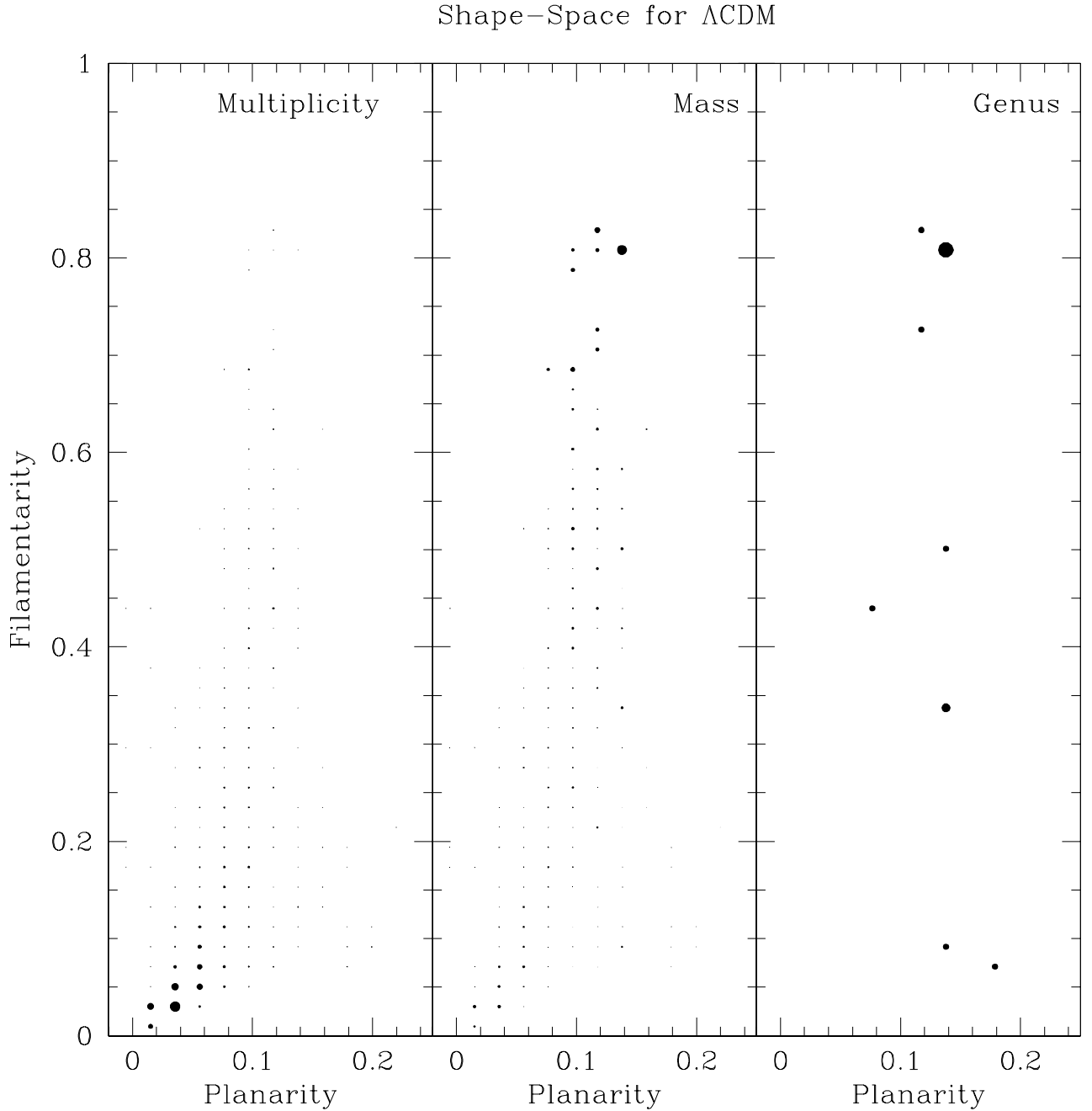


Figure 22. Shape-Space for Λ CDM. Left panel (multiplicity): The dots in this panel have area proportional to the number of clusters with a given (binned) value of Filamentarity and Planarity. Center panel (mass): The dots have area proportional to the total mass contained in clusters having a given (binned) value of Filamentarity and Planarity. Note that more massive superclusters are also more filamentary. Right panel (Genus): The dots have area proportional to the total genus value of superclusters with a given (binned) value of Filamentarity and Planarity. This figure demonstrates the correlation between the mass of a supercluster, its shape and its genus. More massive superclusters are, as a rule, very filamentary and also topologically multiply connected. As in the previous figure, all objects are determined at the percolation threshold.

powerful statistics to discriminate between the models (see Table 4).

To summarize, this paper has demonstrated that Minkowski functionals and Shapefinders evaluated using SURFGEN provide sensitive probes of the geometry, topology and shape

of large scale structure and help in distinguishing between rival cosmological models. Having established the strength and versatility of SURFGEN it would clearly be interesting to apply it to other important issues, related to those addressed in this paper, including: (i) geometry and morphology of underdense regions (voids); (ii) geometry and

morphology of strongly overdense regions (clusters); (iii) redshift-space distortions of supercluster/void morphology; (iv) the time-evolution of the supercluster-void network; (v) analysis of superclusters and voids in fully three dimensional surveys such as 2dFGRS and SDSS; (vi) SURFGEN is also likely to provide useful insights in other physical and astrophysical situations in which matter is distributed anisotropically such as in the interstellar medium (Lazarian & Pogosyan (1996); Boumis, et. al. (2002)). We hope to return to some of these subjects in the near future.

7 ACKNOWLEDGEMENTS

We acknowledge useful discussions with Andrew Benson, Shaun Cole, Suman Datta, Carlos Frenk, Adrian Jenkins, Madan Rao, C.D.Ravikumar, Tarun Deep Saini, Yuri Shtanov, Volker Springel and David Weinberg. Our insights into programming techniques of computational geometry were honed by the excellent monograph on the subject by Joseph O'Rourke. Part of this work was done during a visit of JVS, VS and SS to the Department of Physics & Astronomy, Cardiff University, Cardiff under a PPARC Grant Ref. PPA/V/S/1998/00041. JVS is supported by the research fellowship of the Council of Scientific and Industrial Research (CSIR), India. VS and SS acknowledge support from the Indo-US collaborative project DST/NSF/US (NSF-RP087)/2001. The simulations studied in this paper were carried out by the Virgo Supercomputing Consortium using computers based at Computing Centre of the Max-Planck Society in Garching and at the Edinburgh Parallel Computing Centre. The data are publicly available at www.mpa-garching.mpg.de/NumCos.

REFERENCES

- Arnol'd, V.I., Shandarin, S.F. & Zel'dovich, Ya.B., 1982, *Geophys. Astrophys. Fluid Dynamics*, 20, 111
- Babul, A. and Starkman, G.D., 1992, *ApJ*, 401, 28
- Bahcall, N.A. & Soneira, R.M., 1984, *ApJ*, 277, 27
- Barrow, J.D., Sonoda, D.H. & Bhavsar, S.P., 1985, *MNRAS*, 216, 17
- Basilakos, S., Plionis, M. & Rowan-Robinson, M., 2000, *astro-ph/0007155*.
- Bharadwaj, S., Sahni, V., Sathyaprakash, B.S., Shandarin, S.F., and Yess, C., 2000, *ApJ*, 528, 21.
- Bond, J.R., Kofman, L.A. and Pogosyan, D., 1996, *Nature*, 380, 603.
- Boumis, P., Mavromataki, F., Paleologou, E.V. and Becker, W., 2002, *astro-ph/0209258*.
- Cole, S., Hatton, S., Weinberg, D.H., Frenk, C.S., 1998, *MNRAS*, 945
- de Lapparent, V., Geller, M.J. & Huchra, J.P., 1991, *ApJ*, 369, 273
- Dominik, K.G. & Shandarin, S.F., 1992, *ApJ*, 393, 450
- Gott, J.R., Melott, A.L. & Dickinson, M., 1986, *ApJ*, 306, 341
- Gurbatov, S. N., Saichev, A. I., & Shandarin, S. F. 1985, *Soviet Phys. Dokl.* 30, 921.
- Gurbatov, S. N., Saichev, A. I., & Shandarin, S. F. 1989, *MNRAS* 236, 385.
- Janes, L.G. and Demarque, P., 1983, *ApJ*, 264, 206.
- Jenkins, A.R. et al. (for the Virgo Consortium), 1998, *ApJ*, 499, 20
- Klypin, A.A. & Shandarin, S.F., 1983, *MNRAS*, 204, 891
- Klypin, A.A. & Shandarin, S.F., 1993, *ApJ*, 413, 48
- Luo, S. & Vishniac, E.T., 1995, *ApJS*, 96, 429
- Kofman, L.A., Pogosyan, D., Shandarin, S.F. and Melott, A., 1992, *ApJ*, 393, 450.
- Kolokotronis, V., Basilakos, S. & Plionis, M. 2001, *astro-ph/0111044*
- Lazarian, A. and Pogosyan, D. *astro-ph/9611063*.
- Lorenson, W.E. and Cline, H.E., 1987, *Computer Graphics*, Vol. 21, No. 4, pp 163-169
- Martinez, V.J. and Saar, E. "Statistics of the galaxy distribution", Chapman and Hall.
- Matsubara, T., 2003, *ApJ*, 584, 1
- Mecke, K.R., Buchert, T. & Wagner, H., 1994, *A&A*, 288, 697
- Melott, A.L., 1990, *Phys. Rep.*, 193, 1
- Novikov, D.I., Feldman, H. and Shandarin, S.F., 1999 *Int. J. Mod. Phys.D*, 8, 291
- O'Rourke, J. 1998, *Computational Geometry in C*, 2nd edition (Cambridge Univ. Press)
- Peebles, P.J.E. 1980, *The Large-Scale Structure of the Universe* (Princeton : Princeton Univ. Press)
- Sahni, V. and Coles, P., 1995, *Phys.Rept.*, 262, 1
- Sahni, V., Sathyaprakash, B.S. & Shandarin, S.F., 1998, *ApJL*, 476, L1
- Sahni, V., Sathyaprakash, B.S. & Shandarin, S.F., 1998, *ApJL*, 495, L5
- Sathyaprakash, B.S., Sahni, V. & Shandarin, S.F., 1998, *ApJ*, 508, 551
- Sathyaprakash, B.S., Sahni, V. & Shandarin, S.F., 1996, *ApJL*, 462, L5
- Schaap, W.E. and van de Weygaert, R., 2000, *A & A*, 363, L29-L32
- Schmalzing, J. & Buchert, T., 1997, *ApJL*, 482, L1
- Schmalzing, J. and Gorski, K.M., 1998, *MNRAS*, 297, 355
- Schmalzing, J., Buchert, T., Melott, A.L., Sahni, V., Sathyaprakash, B.S. and Shandarin, S.F., 1999, *ApJ*, 526, 568.
- Shandarin, S.F. & Zeldovich, Ya.B., 1983, *Comments Astrophys.* 10, 33
- Shandarin, S.F. & Zeldovich, Ya.B., 1989, *Rev. Mod. Phys.*, 61, 185
- Shandarin, S.F., Feldman, H.A., Xu, Y., & Tegmark, M., 2002, *ApJS*, 141, 1
- Springel, V. et al. (for the Virgo Consortium), 1998, *MNRAS*, 298, 1169
- van de Weygaert, R., 2002, "Froth across the Universe, Dynamics and Stochastic Geometry of the Cosmic Foam", *arXiv: astro-ph/0206427*
- Yess, C. and Shandarin, S.F., 1996, *ApJ*, 465, 2.
- Zeldovich, Ya.B., Einasto, J. and Shandarin, S.F., 1982, *Nature*, 300, 407.
- Tomita, H., 1990, in *Formation, Dynamics, and Statistics of Patterns*, ed. K. Kawasaki, M. Suzuki, & A. Onuki, Vol. 1 (Singapore: World Scientific), 113

APPENDIX A: GAUSSIAN RANDOM FIELDS AND THE ROLE OF BOUNDARY CONDITIONS

This appendix demonstrates the great accuracy with which SURFGEN determines Minkowski functionals for Gaussian random fields (hereafter GRFs).

Before embarking on our discussion, we briefly describe the samples that we use and summarise the analytical results against which the performance of SURFGEN is to be tested.

We work with three realizations of a gaussian random field with a power law power spectrum ($n = -1$) on a 128^3 grid. Each realization of the field is smoothed with a gaussian kernel of length $\lambda = 2.5$ grid-units. All the fields are normalised by the standard deviation. This leaves them with zero mean and unit variance. The MFs are evaluated at a set of equispaced levels of the density field which coincide with the parameter ν on account of σ being unity ($\rho_{\text{th}} = \nu\sigma = \nu$). ν is used to label the levels and is related to the volume filling fraction through the following equation:

$$FF_V(\nu) = \frac{1}{\sqrt{2\pi}} \int_{\nu}^{\infty} e^{-\frac{t^2}{2}} dt. \quad (\text{A1})$$

The samples are finally used for ensemble averaging.

The Minkowski Functionals (MFs) of a GRF are fully specified in terms of a length-scale λ_c ,

$$\lambda_c = \sqrt{\frac{2\pi\xi(0)}{|\xi''(0)|}}; \quad \sigma^2 = \xi(0). \quad (\text{A2})$$

λ_c can be analytically derived from a knowledge of the power spectrum. It can also be estimated numerically by evaluating the variance $\xi(0)$ of the field and the variance $\xi''(0)$ of any of its first spatial derivatives (for more details see Matsubara 2003).

For a GRF in three dimensions the four MFs (per unit volume) are (Tomita, H. 1990; Matsubara 2003):

$$V(\nu) = \frac{1}{2} - \frac{1}{2}\Phi\left(\frac{\nu}{\sqrt{2}}\right); \quad \Phi(x) = \frac{2}{\sqrt{\pi}} \int_0^{x'} \exp\left(-\frac{x'^2}{2}\right) dx', \quad (\text{A3})$$

where $\Phi(x)$ is the error function.

$$S(\nu) = \frac{2}{\lambda_c} \sqrt{\frac{2}{\pi}} \exp\left(\frac{-\nu^2}{2}\right), \quad (\text{A4})$$

$$C(\nu) = \frac{\sqrt{2\pi}}{\lambda_c^2} \nu \exp\left(\frac{-\nu^2}{2}\right), \quad (\text{A5})$$

$$G(\nu) = \frac{1}{\lambda_c^3 \sqrt{2\pi}} (1 - \nu^2) \exp\left(\frac{-\nu^2}{2}\right). \quad (\text{A6})$$

Let us now describe the boundary conditions which we adopt and which incorporate the periodic nature of the GRFs generated using a FFT routine. GRFs defined on a grid are, by construction, periodic in nature. As a result, two overdense excursion sets visibly separated from each other inside the box and touching two opposite sides of the box would constitute a single cluster. To make this more clear, let us turn to Fig. A1 which shows four clusters (labelled 1, 2, 3 and 4 respectively) in the left panel. The boundaries of these clusters – as drawn by an analog of SURFGEN in 2-D – are shown in bold, and we note that the sides of the box (bold dashed lines) are incorporated when we define the clusters. However, due to the periodicity in the density field, these four clusters are in fact one single cluster (right

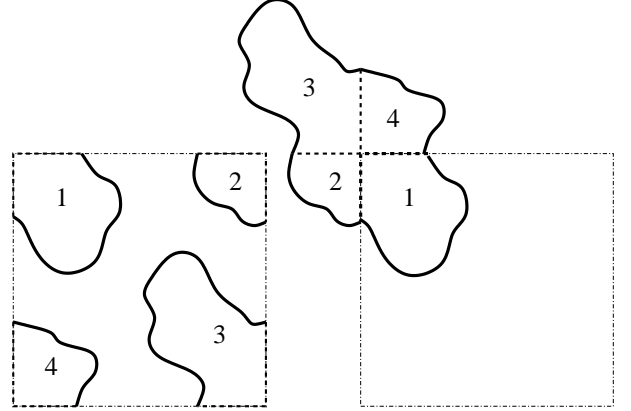


Figure A1. A generic 2-D Gaussian random field with four clusters touching the boundaries of the box is shown in the left panel. SURFGEN-like algorithm in 2-D would treat these as four different contours. However, due to the periodic nature of the GRF, these four clusters in fact constitute a single bigger cluster and the *real* boundaries of the cluster are as shown by bold lines in the right panel of the figure. The dashed solid lines are interior to the cluster and are replaced by 2-dimensional planes in 3-D, which should not be considered in estimating the area and mean curvature. We take care of this effect while estimating MFs for GRFs.

panel). We note that the portion of the contours due to the boundaries of the box occurs in the interior of the actual cluster (shown with a bold dashed line).

It is easy to extrapolate this situation to 3-D. Note that the interpolation method employed by SURFGEN will correctly estimate the global volume of the excursion set even if we worked with the field *as it is*. In 2-D this is same as estimating the area enclosed by the *full* cluster without having to piece the four “clusters” (labelled by 1, 2, 3 and 4) together. Our estimation of global genus will also turn out to be exact, and as it can be shown, this will hold true even if either of these four constituent clusters exhibits a nontrivial topology. On the other hand, if we work with the same set of contours for estimating global area and mean curvature, we will wrongly be adding an excess contribution due to the sides of the box. (In 2-D, this translates to adding the contribution of the dashed line segments to the perimeter of the contour in the right panel of Figure A1). The actual area and mean curvature contribution comes from the interface between overdense and underdense regions (such as the 2-D contours drawn in solid bold line in both the panels) as opposed to the artificial boundaries of the clusters (shown dashed).

We note that incorporating periodic boundary conditions in order to construct a total contour as shown in the right panel of Fig. A1 is nontrivial from the numerical point of view. When the excursion set touches all the boundaries (as, for example, at a very low threshold of density, below the percolation threshold), the corresponding algorithm could further run into an infinite loop, which makes it impractical for implementation. In the light of this, it would be more manageable if we restricted ourselves to using contours which are closed at the boundaries of the box (like the ones in the left panel of Fig. A1), but devise a way to exclude the *excess* contribution to surface area and mean curvature from the

boundaries of the box. A uniform prescription of this type, when applied to all the appropriate clusters at all the thresholds of density will lead to correct estimation of all the global MFs. This then, is the choice of boundary conditions incorporated in our calculation of a GRF. A further cautionary note concerns the familiar W-shape of the genus-curve. Recall that the genus-curve peaks at $\nu = 0$ signifying a sponge-like topology of the medium at the mean density threshold. Note further that $G(\nu = \pm\sqrt{3}) = -2G(0)\exp(-\frac{3}{2})$ are the two negative minima of the genus curve. In fact for $|\nu| > 1$, the genus is *always* negative, and approaches zero from below when $|\nu| \gg 1$. For $\nu < -1$, this negative genus refers to isolated underdense regions (bubbles) in the overdense excursion set. Similarly, the negative genus for $\nu > 1$ should be interpreted as being caused by isolated overdense regions (meatballs) in the underdense excursion set. To summarize, in order to determine the genus for a GRF we need to estimate the genus of the *overdense* excursion set for $\nu \leq 0$ and the genus of the *underdense* excursion set for $\nu > 0$, thereby making use of the symmetry property of the GRFs. (Note however that in our earlier determination of the genus curve for N-body simulations in this paper, we have dealt with the topology of overdense regions only, because of which the genus curve is asymmetric with respect to $\nu = 0$ and is *always positive* when $\nu > 1$.)

Having elaborated on the nature of boundary conditions used in our evaluation of MF's for a GRF, we now present our results.

Figure A2 shows the global MFs averaged over 3 realizations of the density field (solid lines with 1σ error bars) along with the exact analytical results (shown dotted). There are in all 40 levels for every realization. Figure A2 clearly shows the remarkable agreement between exact theoretical results (A3) - (A6) and numerical estimates obtained using SURFGEN. We therefore conclude that SURFGEN determines the MF's of a GRF to great precision.

The above discussion demonstrated the important role played by boundary conditions in reproducing the analytical predictions for GRFs. Having tested the performance of SURFGEN against GRFs, we are faced with the following choice of boundary conditions when dealing with N-body simulations and mock/real galaxy catalogues: (i) we could either correct for the boundaries when dealing with the overdense regions which encounter the faces of the survey-volume, or, (ii) we could avoid doing this and treat all measurements with a tacit understanding that area and mean curvature contain an excess contribution which arises because of boundary effects. Of the two options, the former is computationally more demanding. In addition, its effect is appreciable only significantly after the system has percolated, i.e., when there are a large number of clusters touching the boundaries of the box. The corresponding value of the filling factor ($FF_V > FF_{\text{perc}}$) is useful only when one wishes to compare two samples through the trends in their global MFs. Since the structural elements of the cosmic web (superclusters, voids) are usually identified near the percolation threshold, and are therefore not very sensitive to boundary effects, we have chosen option (ii) in our analysis of N-body simulations in this paper. Option (ii) is also more suited for dealing with real galaxy catalogues which do not satisfy periodic boundary conditions. We should also point out that since we compare two samples under the same conditions –

the same volume and dimensions of the box, same resolution, etc. – the excess contribution to the area and mean curvature caused by box boundaries enters in identical fashion for both the samples. We therefore prefer option (ii) to (i) and all our simulations in Section 5 are analysed without correcting for contributions from the boundaries. (It may also be noted that the contribution from the boundaries becomes less important as we deal with larger survey volumes.)

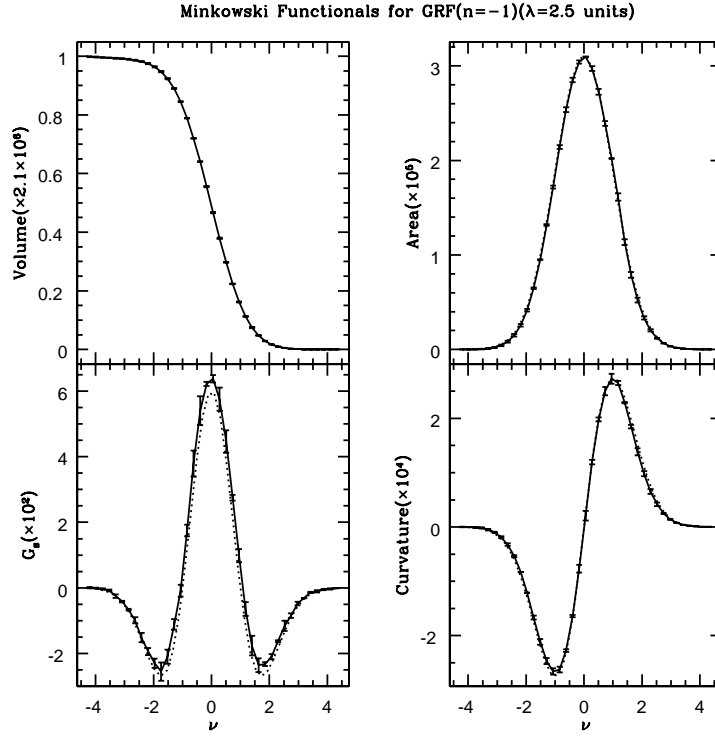


Figure A2. Minkowski Functionals for a GRF ($P(k) \sim k^{-1}$), smoothed with a gaussian filter with $\lambda=2.5$ grid-units. Values of the four Minkowski functionals determined using SURFGEN are shown as solid lines together with the 1σ scatter. Exact analytical results are shown as dotted lines.